Windowed Radon Transform and Tensor Rank-1 Decomposition for Adaptive Beamforming in Ultrafast Ultrasound

Samuel Beuret, *Student Member, IEEE* and Jean-Philippe Thiran, *Member, IEEE*

***Abstract*— Ultrafast ultrasound has recently emerged as an alternative to traditional focused ultrasound. By virtue of the low number of insonifications it requires, ultrafast ultrasound enables the imaging of the human body at potentially very high frame rates. However, unaccounted for speed-of-sound variations in the insonified medium often result in phase aberrations in the reconstructed images. The diagnosis capability of ultrafast ultrasound is thus ultimately impeded. Therefore, there is a strong need for adaptive beamforming methods that are resilient to speed-of-sound aberrations. Several of such techniques have been proposed recently but they often lack parallelizability or the ability to directly correct both transmit and receive phase aberrations. In this article, we introduce an adaptive beamforming method designed to address these shortcomings. To do so, we compute the windowed Radon transform of several complex radio-frequency images reconstructed using delay-and-sum. Then, we apply to the obtained local sinograms weighted tensor rank-1 decompositions and their results are eventually used to reconstruct a corrected image. We demonstrate using simulated and in-vitro data that our method is able to successfully recover aberration-free images and that it outperforms both coherent compounding and the recently introduced SVD beamformer. Finally, we validate the proposed beamforming technique on in-vivo data, resulting in a significant improvement of image quality compared to the two reference methods.**

***Index Terms*— Aberration Correction, Adaptive Beamforming, Ultrafast Ultrasound**

I. Introduction

In the last 20 years, ultrafast ultrasound has emerged as a new paradigm rivalling traditional focused ultrasound [1]. It relies on the emission of unfocused waves by an ultrasound transducer. The recorded echoes are then synthetically focused to recover an image estimating the reflectivity of the human soft tissues. To improve the image quality, images corresponding to different insonifications can then be combined into one, most commonly using coherent compounding [2]. Due to the high frame-rate the method allows, ultrafast ultrasound has enabled new diagnostic techniques such as shear-waves elastography [3]–[5] or neurofunctional imaging [6], among others.

Paper submitted for reviews on June 30th 2023.

Samuel Beuret and Jean-Philippe Thiran are with the Signal Processing Laboratory 5 at the École polytechnique fédérale de Lausanne (EPFL), Lausanne, Switzerland (e-mails: samuel.beuret@epfl.ch, jean-philippe.thiran@epfl.ch).

Jean-Philippe Thiran is also with the Department of Radiology, University Hospital Center and University of Lausanne, Lausanne, Switzerland.

To reconstruct an image, ultrafast ultrasound—as well as traditional focused ultrasound—presupposes a constant speed of sound (SoS) in the imaged tissues. This hypothesis is however not met in practice since the SoS of human soft tissues can vary up to the order of 10% and beyond [7]. In effect, SoS variations introduce high-order aberrations in the reconstructed images that are ultimately detrimental to the diagnostic capability of ultrasound imaging [8], [9]. Therefore, there exists a strong impetus to design image reconstruction techniques that are resilient to aberrations induced by SoS variations.

Numerous aberration correction methods have thus been proposed throughout the development of ultrasound imaging [10]–[12]. A large part of these methods posits the existence of a thin aberrating layer in front of the transducer. Angular aberrations are therefore supposed constant in the medium. This hypothesis is justified in specific imaging configurations. In general, however, such methods fail to address the aberrations generated by a spatially varying SoS distribution.

The recent years have witnessed the development of pulse-echo SoS imaging methods [13]–[16]. Their goal is to reconstruct a map of the local SoS from pulse-echo ultrasound measurements. To correct for SoS aberrations, propagation delays can be deduced from the imaged SoS and then used by delay-and-sum (DAS) and coherent compounding to reconstruct an image [17], [18]. Especially relevant to our work is the method presented in [19], where directional filters applied to beamformed images are used to take into account aberrations. Several drawbacks of this general approach can however be highlighted. First, such methods do not allow a gain of performance compared to DAS in the absence of aberrations. In particular, they do not alleviate diffraction—side lobes, grating lobes—artifacts and multiple scattering artifacts. Second, local SoS recovery currently lacks robustness, which may lead to errors in the propagation delays estimation. Finally, the estimation of SoS at a specific point in the medium requires the knowledge of aberration delays from the entire medium. This fact prevents the parallelization of such methods with respect to zones of interest. The SoS recovery from local aberration delays is furthermore a computationally demanding operation and those two facts currently prevent real-time implementations of pulse-echo SoS imaging methods.

In contrast, novel approaches have emerged recently to better exploit the coherence existing between insonifications. These methods provide an increased robustness against SoS

aberrations along with other artifacts such as diffraction and multiple scattering artifacts. The SVD beamformer introduced in [20], [21] is especially relevant to our work. Its basic principle is to beamform using DAS a series of complex radio-frequency (CRF) images—one per insonification—and extract patches from them. A stack of patches can be interpreted as a matrix and its leading right singular vector corresponds to a patch of the corrected image. In addition, the leading left singular vector corresponds to local aberrations and can be used to estimate local SoS [22]. Computationally light and easily parralelizable, SVD beamforming is however only able to directly correct for transmit (Tx) aberrations. Receive (Rx) aberrations are overlooked, penalizing in practice the performances of the method. Another proposed approach exploiting redundancy between insonifications is ultrasound matrix imaging (UMI) [23], [24]. This technique constructs virtual emitters and receivers in the imaged medium. Aberration correction—among other features of UMI—is performed by maximizing the energy of emitters-receivers pairs when placed at the same location. However, the construction of the corrected focused reflection matrix in UMI-based aberration correction is a complex operation that must be iterated, hindering in practice computation time of the method. In addition, we can cite the locally adaptive Tx-Rx phase correction method proposed in [25]. Full-synthetic-aperture data are acquired and the local Tx phase aberrations associated with each element are computed from beamformed images. The estimated aberration phases are used to correct both Tx and Rx aberrations, thus obtaining a new image, and this procedure is ultimately iterated. However, the iterative process and the reliance on full-synthetic-aperture data negatively impacts the computational complexity of the method. Furthermore it is unable to provide any image improvement beside the correction of phase aberrations.

Therefore, our goal in this article is to propose an adaptive beamforming method for ultrafast ultrasound that adheres to the following guidelines:

- It should be able to simultaneously correct for spatially-varying Tx and Rx phase aberrations,
- It should also provide additional robustness to artifacts such as multiple scattering and diffraction artifacts with respect to coherent compounding,
- It should be easily parallelizable and thus avoid to iteratively reconstruct images or to compute a local SoS map.

To do so, we rely on the concept of change of basis from the canonical sensor basis to a Rx plane waves (PWs) basis—sometimes denoted as Radon domain—proposed recently or ultrasound pulse-echo imaging [26]–[28]. Following [20], [24], the main rationale behind the proposed method is to express the data into a local Rx PW basis to account for the locality of the phase aberrations induced by SoS variations.

II. Theory

In this section, we first describe the model of the received signals. Then, we detail the theoretical argument underpinning the proposed method.

A. Signal Model and Beamforming

In this article, we restrict ourselves to the case of a linear transducer. We suppose that it is aligned with the x axis and that waves are emitted towards the positive z direction. An element of the transducer is then defined by its position $\boldsymbol{r}^{\mathrm{el}} = [x^{\mathrm{el}}, 0]^T$. Furthermore, we assume that the transducer emits N^{Tx} PWs parametrized by their steering angles θ^{Tx}. According to [29], we model the CRF echo-signal m received by an arbitrary sensor when an arbitrary steered PW is emitted as

$$m\left(\theta^{\mathrm{Tx}}, x^{\mathrm{el}}, t\right) = v_{\mathrm{pe}}(t) *_t \int_{\boldsymbol{r}} \left[\tilde{h}^{\mathrm{Tx}}\left(\theta^{\mathrm{Tx}}, \boldsymbol{r}, t\right) *_t \tilde{h}^{\mathrm{Rx}}\left(x^{\mathrm{el}}, \boldsymbol{r}, t\right)\right] \gamma(\boldsymbol{r})\, \mathrm{d}\boldsymbol{r}, \quad (1)$$

where the functions $\tilde{h}^{\mathrm{Tx}}$ and $\tilde{h}^{\mathrm{Rx}}$ designate the Tx and Rx spatial impulse responses (SIRs), respectively, and $*_t$ represents a temporal convolution. We denote by v_{pe} the pulse-echo waveform accounting for the electro-acoustic (Tx) impulse response, acousto-electric (Rx) impulse response and electric excitation waveform. We represent by γ the tissue reflectivity function (TRF) which factors in the local fluctuations of density and SoS generating scattered echo signals.

Following [30], [31], we introduce Tx and Rx far-field approximations. The convolutions with the SIRs $\tilde{h}^{\mathrm{Tx/Rx}}$ in (1) are therefore approximated by the composition of a spatial multiplication with a function $h^{\mathrm{Tx/Rx}}$ and a temporal shift according to the Tx/Rx wave propagation time. Moreover, we assume that v_{pe} is a complex analytic signal with center frequency $f_0 = \omega_0/2\pi$. Under these assumptions, we can rewrite (1) as

$$m\left(\theta^{\mathrm{Tx}}, x^{\mathrm{el}}, t\right) = \int_{\boldsymbol{r}} h^{\mathrm{Tx}}\left(\theta^{\mathrm{Tx}}, \boldsymbol{r}\right)\, h^{\mathrm{Rx}}\left(x^{\mathrm{el}}, \boldsymbol{r}\right) e^{-j\omega_0 \Delta\tau^{\mathrm{Tx}}\left(\theta^{\mathrm{Tx}}, \boldsymbol{r}\right)} e^{-j\omega_0 \Delta\tau^{\mathrm{Rx}}\left(x^{\mathrm{el}}, \boldsymbol{r}\right)} v_{\mathrm{pe}}\Big(t - \tau^{\mathrm{Tx}}\left(\theta^{\mathrm{Tx}}, \boldsymbol{r}\right) - \tau^{\mathrm{Rx}}\left(x^{\mathrm{el}}, \boldsymbol{r}\right)\Big) \gamma(\boldsymbol{r})\, \mathrm{d}\boldsymbol{r}. \quad (2)$$

Here, the functions h^{Tx} and h^{Rx} are assumed real and positive and they factor in element directivity, decay and attenuation. In (2), we split the Tx and Rx propagation times into two distinct terms: the expected propagation times τ^{Tx}, τ^{Rx} and the aberrations delays $\Delta\tau^{\mathrm{Tx}}$, $\Delta\tau^{\mathrm{Rx}}$. In-line with previous works on SoS estimation and aberration correction [15], [19], [20], we reduce the effect of aberration delays to phase shifts by assuming that v_{pe} is narrow-band.

We compute the expected propagation times by positing a uniform SoS c_0 in the medium. The Tx propagation times are then given by

$$\tau^{\mathrm{Tx}}\left(\theta^{\mathrm{Tx}}, \boldsymbol{r}\right) = \frac{1}{c_0}\left\langle \boldsymbol{u}\left(\theta^{\mathrm{Tx}}\right), \boldsymbol{r}\right\rangle, \text{ with } \boldsymbol{u}\left(\theta\right) = \begin{bmatrix}\sin(\theta)\\ \cos(\theta)\end{bmatrix}, \quad (3)$$

since we assume that the time origin $t = 0$ is defined as the instant when the wave is emitted from the point $\boldsymbol{r} = 0$ located at the center of the transducer. Furthermore, the Rx propagation times are given by

$$\tau^{\mathrm{Rx}}\left(x^{\mathrm{el}}, \boldsymbol{r}\right) = \frac{1}{c_0}\left\|\boldsymbol{r} - \boldsymbol{r}^{\mathrm{el}}\right\|. \quad (4)$$

Aberration delays $\Delta\tau^{\mathrm{Tx/Rx}}$ are therefore the result of a mismatch between the physical local SoS and the assumed SoS c_0.

We now suppose that DAS is applied independently to the data obtained with each PW insonification. Moreover, we assume that we have access to a continuous range of sensor positions $x^{\mathrm{el}} \in \left[-x^{\max}, x^{\max}\right]$. Under this hypothesis, DAS can be expressed as

$$y^{\mathrm{DAS}}\left(\theta^{\mathrm{Tx}}, \boldsymbol{r}'\right) = \int_{x^{\mathrm{el}}=-x^{\max}}^{x^{\max}} a^{\mathrm{Tx}}\left(\theta^{\mathrm{Tx}}, \boldsymbol{r}'\right)\, a^{\mathrm{Rx}}\left(x^{\mathrm{el}}, \boldsymbol{r}'\right) m\left(\theta^{\mathrm{Tx}}, x^{\mathrm{el}}, \tau^{\mathrm{Tx}}\left(\theta^{\mathrm{Tx}}, \boldsymbol{r}'\right) + \tau^{\mathrm{Rx}}\left(x^{\mathrm{el}}, \boldsymbol{r}'\right)\right) \mathrm{d}\boldsymbol{r}, \quad (5)$$

where a^{Tx} and a^{Rx} denote real and positive apodization weights. In particular, the sensor continuum hypothesis has the practical effect of neglecting grating lobes altogether. The resulting expression y^{DAS} is a function of both the spatial position in the image $\boldsymbol{r}'$ and the Tx angle θ^{Tx}.

B. Local Angular Framework

To deepen our analysis, we focus on the vicinity $\mathbb{V}(\boldsymbol{r}^{\mathrm{w}})$ of a point $\boldsymbol{r}^{\mathrm{w}} = [x^{\mathrm{w}}, z^{\mathrm{w}}]^T$ in the image series y^{DAS}. We first suppose that $a^{\mathrm{Tx/Rx}}$, $h^{\mathrm{Tx/Rx}}$, and $\Delta\tau^{\mathrm{Tx/Rx}}$ vary slowly in the medium and thus can be assumed constant in $\mathbb{V}(\boldsymbol{r}^{\mathrm{w}})$ and equal to their value at $\boldsymbol{r}^{\mathrm{w}}$. In that regard, $\mathbb{V}(\boldsymbol{r}^{\mathrm{w}})$ is equivalent to the isoplanatic patch used in [20], [23]. Importantly, we posit that the reflectivity γ is null outside of $\mathbb{V}(\boldsymbol{r}^{\mathrm{w}})$. We will address in Section III-C how to enforce this hypothesis in practice.

First of all, we introduce a local Rx angle

$$\theta^{\mathrm{Rx}} = \arctan\left(\frac{x^{\mathrm{w}} - x^{\mathrm{el}}}{z^{\mathrm{w}}}\right), \quad (6)$$

and re-express each function of x^{el} as a function of θ^{Rx}. Second, we posit that the Rx expected propagation time can be assumed linear within $\mathbb{V}(\boldsymbol{r}^{\mathrm{w}})$ and expressed as:

$$\tau^{\mathrm{Rx}}(\theta^{\mathrm{Rx}}, \boldsymbol{r}) \approx \frac{1}{c_0}\left\langle \boldsymbol{u}\left(\theta^{\mathrm{Rx}}\right), \boldsymbol{r} - \boldsymbol{r}^{\mathrm{w}}\right\rangle + \frac{z^{\mathrm{w}}}{c_0 \cos\left(\theta^{\mathrm{Rx}}\right)}, \quad (7)$$

with $\boldsymbol{u}(\theta)$ the vector defined in (3). Equation (7) stems from the first order Taylor expansion of (4) around $\boldsymbol{r}^{\mathrm{w}}$, combined with the change of variable introduced in (6).

Lastly, we assume the following hypothesis

$$\cos\left(\frac{\theta^{\mathrm{Tx}} - \theta^{\mathrm{Rx}}}{2}\right) \approx 1, \quad (8)$$

which holds true even for large difference between θ^{Tx} and θ^{Rx} (10% of error for a 52° difference).

Let us now define the Radon transform $\mathcal{R}$ of an arbitrary two-dimensional function g:

$$\mathcal{R}_{(\boldsymbol{r})}\left\{g(\boldsymbol{r})\right\}(\theta, d) = \int_{\boldsymbol{r}} g(\boldsymbol{r})\delta\left(\left\langle \boldsymbol{u}(\theta), \boldsymbol{r}\right\rangle - d\right) \mathrm{d}\boldsymbol{r}, \quad (9)$$

with $\boldsymbol{u}$ a unitary vector in the direction given by θ (3), and d the distance along $\boldsymbol{u}$ with respect to $\boldsymbol{r} = 0$. We define its adjoint operator $\mathcal{R}^*$, often designated as *backprojection*, applied to a function h as

$$\mathcal{R}^*_{(\theta,d)}\{h(\theta, d)\}(\boldsymbol{r}) = \int_{\theta} h\left(\theta, \left\langle \boldsymbol{u}(\theta), \boldsymbol{r}\right\rangle\right) \mathrm{d}\theta. \quad (10)$$

Factoring in (2), the hypotheses introduced in this section, and the definition of the adjoint Radon transform $\mathcal{R}^*$, we can rewrite (5) as:

$$y^{\mathrm{DAS}}\left(\theta^{\mathrm{Tx}}, \boldsymbol{r}'\right) = \mathcal{R}^*_{(\theta^{\mathrm{mid}}, d)}\left\{s\left(\theta^{\mathrm{Tx}}, 2\theta^{\mathrm{mid}} - \theta^{\mathrm{Tx}}, d\right)\right\}\left(\boldsymbol{r}' - \boldsymbol{r}^{\mathrm{w}}\right), \quad (11)$$

with

$$s\left(\theta^{\mathrm{Tx}}, \theta^{\mathrm{Rx}}, d\right) = l^{\mathrm{Tx}}\left(\theta^{\mathrm{Tx}}\right) l^{\mathrm{Rx}}\left(\theta^{\mathrm{Rx}}\right) f\left(\frac{\theta^{\mathrm{Tx}} + \theta^{\mathrm{Rx}}}{2}, d\right), \quad (12)$$

a series of sinograms, one per combination of Tx angle θ^{Tx} and window position $\boldsymbol{r}^{\mathrm{w}}$. Here, d represents the distance to the center of the patch $\boldsymbol{r}^{\mathrm{w}}$ along $\boldsymbol{u}$. Also, we introduce in (11) the *mid angle*

$$\theta^{\mathrm{mid}} = \frac{\theta^{\mathrm{Tx}} + \theta^{\mathrm{Rx}}}{2}, \quad (13)$$

which corresponds to the average between the Tx and Rx angles. In (12), we denote by $l^{\mathrm{Tx/Rx}}$ two apodization/aberration functions defined as

$$\begin{aligned} l^{\mathrm{Tx}}\left(\theta^{\mathrm{Tx}}\right) &= a^{\mathrm{Tx}}\left(\theta^{\mathrm{Tx}}\right) h^{\mathrm{Tx}}\left(\theta^{\mathrm{Tx}}\right) e^{-j\omega_0 \Delta\tau\left(\theta^{\mathrm{Tx}}\right)}, \\ l^{\mathrm{Rx}}\left(\theta^{\mathrm{Rx}}\right) &= \frac{z^{\mathrm{w}}}{\cos^2\left(\theta^{\mathrm{Rx}}\right)} a^{\mathrm{Rx}}\left(\theta^{\mathrm{Rx}}\right) h^{\mathrm{Rx}}\left(\theta^{\mathrm{Rx}}\right) e^{-j\omega_0 \Delta\tau\left(\theta^{\mathrm{Rx}}\right)}, \end{aligned} \quad (14)$$

since the Tx and Rx aberrations delays $\Delta\tau^{\mathrm{Tx}} = \Delta\tau^{\mathrm{Rx}} = \Delta\tau$ are equal when expressed in the same angular basis. Note that there is an implicit dependency of θ^{Rx}, $a^{\mathrm{Tx/Rx}}$, $h^{\mathrm{Tx/Rx}}$, and $\Delta\tau$, and therefore of $l^{\mathrm{Tx/Rx}}$, f and s, to $\boldsymbol{r}^{\mathrm{w}}$, omitted here for conciseness. Furthermore, the additional term appearing in the definition of l^{Rx} compared to l^{Tx} stems from the change of variable (6) applied to the integral (5). In the definition of s (12), f denotes a term factoring in the reflectivity and the pulse-echo waveform. In fact, f represents the Radon transform of an unapodized image free of aberrations restricted to $\mathbb{V}(\boldsymbol{r}^{\mathrm{w}})$. Importantly, we must highlight that f is a function of the mid angle. The definition of f and the computation of (11) are detailed in Appendix I. The proposed mathematical framework is inspired by [13], [23]. In particular, the importance of the mid-angle in the proposed framework can be traced back to the latter article.

Therefore, our proposition for an adaptive beamforming method can be summarized as follows. We reconstruct using DAS a series y^{DAS} of one image per insonification. These images are divided into zones (or patches) $\mathbb{V}(\boldsymbol{r}^{\mathrm{w}})$ to abide by the strong hypotheses introduced in this section. For each zone $\mathbb{V}(\boldsymbol{r}^{\mathrm{w}})$ we estimate first function s, then function f. Ultimately, function f is used to reconstruct an aberration-free image restricted to $\mathbb{V}(\boldsymbol{r}^{\mathrm{w}})$ and the local images obtained for different zones are combined into a single one.

III. Method

In this section, we present the practical aspects of the proposed method. We first detail the data acquisition and beamforming processes. We describe thereafter which patches $\mathbb{V}(\boldsymbol{r}^{\mathrm{w}})$ to select and how to obtain s for each patch, followed by the computation of f using tensor rank-1 decomposition. Finally, we present the reconstruction of the image, along with our implementation of the SVD beamformer used as a reference method.

TABLE I
TRANSDUCER AND SEQUENCE

Transducer	GE9L-D
Number of elements N^{el}	192
Pitch	230 µm
Aperture	43.93 mm
Element width	0.9·230 µm[a]
Element height	6 mm
Elevation focus	28 mm
Center frequency	5.3 MHz
Fractional bandwidth	75%
Steering angle spacing	5°
Number of insonifications N^{Tx}	9
Excitation cycles	1
Excitation frequency f_0	5.2 MHz
Sampling frequency f_s	20.8 MHz
Pulse repetition frequency	9 kHz

[a]No official data available, guessed value according to [32]

A. Acquisition

All experimental data considered throughout this article have been acquired using a GE9L-D ultrasound transducer (GE Healthcare, Chicago, Illinois, USA) connected to a Vantage 256 system (Verasonics, Kirkland, WA, USA). In addition, a geometric model of the transducer has been used in numerical simulations. The transducer comprises a series of $N^{\mathrm{el}} = 192$ discrete sensors with positions $\boldsymbol{x}^{\mathrm{el}} \in \mathbb{R}^{N^{\mathrm{el}}}$. We consider a Tx sequence consisting of N^{Tx} PWs with uniformly spaced steering angles $\boldsymbol{\theta}^{\mathrm{Tx}} \in \mathbb{R}^{N^{\mathrm{Tx}}}$, where $N^{\mathrm{Tx}} = 9$ and $\boldsymbol{\theta}^{\mathrm{Tx}} = -20°, -15°, ..., 20°$ unless stated otherwise. The echo signals are recorded using all N^{el} elements for each insonification. We directly apply the Hilbert transform to the raw measurements so that they can be described by a series of analytic signals gathered into a vector $\boldsymbol{m} \in \mathbb{C}^{N^{\mathrm{Tx}} N^{\mathrm{el}} N^{\mathrm{t}}}$. N^{t} denotes here the number of time samples considered after sampling the recieved signals with frequency f_s. The specifications of the transducer and sequence are summarized in Table I.

B. Delay-and-Sum

Given the measurements $\boldsymbol{m}$, we use DAS to compute the beamformed PW images y^{DAS}. In practice, we discretize (5) as a sum over all sensors x^{el} and we interpolate cubically between time samples. Function y^{DAS} is estimated at a series of points $\boldsymbol{r}' = [x'_m, z'_n]^T$, $m = 1, ..., N^x$, $n = 1, ..., N^z$. Therefore, it is represented by a vector $\boldsymbol{y}^{\mathrm{DAS}} \in \mathbb{C}^{N^{\mathrm{Tx}} N^x N^z}$.

To ease the implementation of the proposed method, we use an isotropic grid with spatial spacings $\Delta x' = \Delta z' = c_0/(8 f_0) = 38.5$ µm selected to guarantee a 200% fractional bandwidth [33]. The Tx apodization a^{Tx} is set to 1 whereas a Tukey apodization with 42° half-aperture and 0.15 cosine fraction is used as the Rx apodization a^{Rx} to reduce grating lobe level.

We choose a 42° half-aperture because it corresponds to the angle at which the directivity of the element reaches 6dB below its maximum value. Assuming a soft baffle boundary condition, we compute the theoretical angular directivity of a narrow element in the far field according to [34], considering the element width given in Table I.

C. Windowed Radon Transform

As detailed in Section II-B, beamformed images y^{DAS} must be restricted to a series of patches $\mathbb{V}(\boldsymbol{r}^{\mathrm{w}})$. Practically, we thus window y^{DAS} with a function w shifted by a series of vectors $\boldsymbol{r}^{\mathrm{w}}$, such that $\boldsymbol{r}^{\mathrm{w}}$ represents the center of the window and $\mathbb{V}(\boldsymbol{r}^{\mathrm{w}}) = \{\boldsymbol{r}' : \ w(\boldsymbol{r}' - \boldsymbol{r}^{\mathrm{w}}) > 0\}$.

To estimate function s for a specific window position $\boldsymbol{r}^{\mathrm{w}}$, we can insert the windowing operation into (11). The result can be rewritten as

$$w(\boldsymbol{r}' - \boldsymbol{r}^{\mathrm{w}})\, y^{\mathrm{DAS}}(\theta^{\mathrm{Tx}}, \boldsymbol{r}') = \mathcal{R}^*_{(\theta^{\mathrm{mid}}, d)} \left\{ s(\theta^{\mathrm{Tx}}, 2\theta^{\mathrm{mid}} - \theta^{\mathrm{Tx}}, d) \right\} (\boldsymbol{r}' - \boldsymbol{r}^{\mathrm{w}}), \ \forall \theta^{\mathrm{Tx}}. \quad (15)$$

The inverse of the Radon transform is given by filtered backprojection, the composition of a filtering self-adjoint operator $\mathcal{F}$ and the adjoint of the Radon transform $\mathcal{R}^*$ [35], namely

$$\mathcal{R}^{-1} = \mathcal{R}^* \mathcal{F} \iff [\mathcal{R}^*]^{-1} = \mathcal{F}\mathcal{R}. \quad (16)$$

Equation (15) can thus be further re-expressed as

$$s(\theta^{\mathrm{Tx}}, \theta^{\mathrm{Rx}}, d) = \mathcal{F}\mathcal{R}_{(\tilde{\boldsymbol{r}})} \left\{ w(\tilde{\boldsymbol{r}}) y^{\mathrm{DAS}}(\theta^{\mathrm{Tx}}, \tilde{\boldsymbol{r}} + \boldsymbol{r}^{\mathrm{w}}) \right\} \left(\tfrac{\theta^{\mathrm{Tx}} + \theta^{\mathrm{Rx}}}{2}, d \right), \ \forall \theta^{\mathrm{Tx}}, \quad (17)$$

with $\tilde{\boldsymbol{r}} = \boldsymbol{r}' - \boldsymbol{r}^{\mathrm{w}}$. We define the filtering operator $\mathcal{F}$ applied to an arbitrary function $g(d)$ as

$$\mathcal{F}\{\hat{g}\}(\zeta) = \frac{1}{4\pi^2} |\zeta| \hat{g}(\zeta) \quad (18)$$

in the frequency domain, with $\hat{g}$ the Fourier transform of g and ζ the spatial frequency associated with d. Equation (17) without the filtering operation is known as a *windowed Radon transform* [36].

In practice, we introduce a set of N^{Rx} discrete uniformly spaced Rx angles θ^{Rx}_j, $j = 1, ..., N^{\mathrm{Rx}}$ to evaluate (17), and we consider N^d values of d such that the spatial spacing of d is equal to the spatial grid spacing of the image $\Delta x' = \Delta z'$. Furthermore, we consider a discrete grid of window centers $\boldsymbol{r}^{\mathrm{w}}_{q,p}$ such that $p = 1, ..., N^{\mathrm{w},x}$, $q = 1, ..., N^{\mathrm{w},z}$, with $N^{\mathrm{w},x}$, $N^{\mathrm{w},z}$ the number of points in the x and z directions. The distance between two window centers is set to $\Delta x^{\mathrm{w}} = \Delta z^{\mathrm{w}} = 24\Delta x = 0.924$ mm to ensure a three quarters overlap between windows since a sufficient overlap is necessary in the image reconstruction step—c.f. Section III-E—. Finally, we implement (18) as a filter in the spatial domain to recover a *bona fide* estimation of s from the result of the windowed Radon transform.

It is important to mention that the mathematical analysis detailed in Section II-B neglects the windowing of the image introduced in (17). A side effect of the windowing is the limitation of the angular resolution of s with respect to θ^{Rx} due to the convolution in the frequency domain between the the 2D spectrum of the window and the spectra of the images y^{DAS}. To minimize this phenomenon, one must choose a window w with a narrow main lobe. Furthermore, the window must must be smooth to avoid artifacts in the reconstruction—c.f. Section III-E—. Thus, a Tukey window with 0.5 cosine fraction is chosen as a trade-off. The radius R^{w} must also achieve a critical trade-off. It needs to be sufficiently small to enforce the

hypotheses introduced in Section II-B, but large enough to be resilient to local TRF variations. We determined empirically that $R^{\mathrm{w}} = 52\Delta x = 2\,\mathrm{mm}$ provides a good compromise for the proposed imaging configuration.

In turn, the Rx angular spacing is constrained by the size of the window. This constraint stems from the necessity to sample the whole 2D frequency plane. If this condition is not met, strong local grating lobe artifacts can appear in the reconstructed image. Let us recall that the main lobe width of a 2D Tukey window with radius R^{w} and 0.5 cosine fraction is $f^{\mathrm{w}} = 0.902/R^{\mathrm{w}}$. We posit that the minimum distance between two samples in the frequency plane must be at most equal to the window main lobe width. In accordance with the size of the image grid, we need to guarantee a 200% fractional bandwith. Therefore, the maximum 2D spatial frequency magnitude we must consider is $f^{\max} = 2 \cdot 2f_0/c_0$. Under a small angle hypothesis, the maximum angular spacing of the mid angle is then given by $f^{\mathrm{w}}/f^{\max} = 0.033 = 1.91°$. According to (17), there is a one-half factor between the mid angle and the Rx angle, the maximum Rx angular spacing is consequently 3.82°. Regarding the maximum Rx angle, we set it such that it corresponds to the last angle not affected by the Rx apodization a^{Rx}, namely $(1 - 0.15)\cdot 42° \approx 35°$.

D. Tensor Rank-1 Decomposition

To recover $l^{\mathrm{Tx/Rx}}$ and f from s, we propose to solve the following inverse problem

$$\min_{f,\ \|l^{\mathrm{Tx}}\|_{\Omega^{\mathrm{Tx}}}=1,\ \|l^{\mathrm{Rx}}\|_{\Omega^{\mathrm{Rx}}}=1} \frac{1}{2}\left\|l^{\mathrm{Tx}} l^{\mathrm{Rx}} f^{\mathrm{Tx,Rx}} - s\right\|^2_{\Omega^{\mathrm{Tx}}\times\Omega^{\mathrm{Rx}}\times\Omega^d} + \frac{\mu}{2}\left\|f\right\|^2_{\Omega^{\mathrm{mid}}\times\Omega^d}, \quad (19)$$

with

$$\left\|l^{\mathrm{Tx/Rx}}\right\|^2_{\Omega^{\mathrm{Tx/Rx}}} = \int_{\theta^{\mathrm{Tx/Rx}}\in\Omega^{\mathrm{Tx/Rx}}} \left|l^{\mathrm{Tx/Rx}}\left(\theta^{\mathrm{Tx/Rx}}\right)\right|^2 \mathrm{d}\theta^{\mathrm{Tx/Rx}}, \quad (20)$$

$$\left\|f\right\|^2_{\Omega^{\mathrm{mid}}\times\Omega^d} = \iint_{\theta^{\mathrm{mid}}\in\Omega^{\mathrm{mid}},d\in\Omega^d} \left|f\left(\theta^{\mathrm{mid}},d\right)\right|^2 \mathrm{d}\theta\,\mathrm{d}d, \quad (21)$$

$$\left\|g\right\|^2_{\Omega^{\mathrm{Tx}}\times\Omega^{\mathrm{Rx}}\times\Omega^d} = \iiint_{\theta^{\mathrm{Tx}}\in\Omega^{\mathrm{Tx}},\theta^{\mathrm{Rx}}\in\Omega^{\mathrm{Rx}},d\in\Omega^d} \left|g\left(\theta^{\mathrm{Tx}},\theta^{\mathrm{Rx}},d\right)\right|^2 \mathrm{d}\theta^{\mathrm{Tx}}\,\mathrm{d}\theta^{\mathrm{Rx}}\,\mathrm{d}d, \quad (22)$$

for an arbitrary function g, and

$$f^{\mathrm{Tx,Rx}}\left(\theta^{\mathrm{Tx}},\theta^{\mathrm{Rx}},d\right) = f\left(\frac{\theta^{\mathrm{Tx}}+\theta^{\mathrm{Rx}}}{2},d\right). \quad (23)$$

In (19), $\Omega^{\mathrm{Tx/Rx}}$, Ω^{mid}, and Ω^d denote the ranges of $\theta^{\mathrm{Tx/Rx}}$, θ^{mid}, and d, respectively. Problem (19) can be interpreted as a weighted and regularized rank-1 canonical polyadic (CP) decomposition in the continuous domain.

The regularization term is necessary to prevent a divergence of the solution, for instance if l^{Tx} and l^{Rx} are null for certain angles. In fact, the regularization term enables a dynamical apodization of the image. A small regularization parameter μ implies that the proposed method compensates for the angular directivity of the sensors, among other magnitude effects acting on the received signals. Lateral resolution is thus typically favored at the expense of robustness to multiple scattering and diffraction artifacts. The opposite phenomenon occurs when a large regularization parameter μ is chosen. The proposed method is then more robust to artifacts at the expense of lateral resolution. We determined empirically that $\mu = 1$ provides a good trade-off—c.f. Section IV-B—. It can be tuned in practice if the user wants to favor contrast or lateral resolution. The adaptive apodization of the proposed method extends in effect the Tx adaptive apodization already enforced by SVD beamforming. As presented in Section I, one of the goal of the proposed method is to provide an increase in performance compared to coherent compounding, even in the absence of aberrations. This improvement—of contrast, especially—is permitted in practice by the mechanism of adaptive apodization detailed above. In that regard, the proposed method shares strong similarities with minimum variance beamforming [37], [38]. Problem (19) can be interpreted as finding the weights $\boldsymbol{l}^{\mathrm{Tx}}$ and $\boldsymbol{l}^{\mathrm{Rx}}$ minimizing the variance of all the signals sharing the same mid angle, and the effect of the regularizer is akin to diagonal loading of the covariance matrix.

We solve (19) with alternating least-squares (ALS), a common method for CP decomposition [39]. Its fundamental principle is to solve least-squares problems by fixing alternatively two out of the three variables f, l^{Tx}, and l^{Rx}. The ALS scheme with continuous signals is detailed in Algorithm 1, where $\bar{\cdot}$ denotes the complex conjugate. In practice, the main ALS loop solves the following unconstrained problem

$$\min_{f,l^{\mathrm{Tx}},l^{\mathrm{Rx}}} \frac{1}{2}\left\|l^{\mathrm{Tx}} l^{\mathrm{Rx}} f^{\mathrm{Tx,Rx}} - s\right\|^2_{\Omega^{\mathrm{Tx}}\times\Omega^{\mathrm{Rx}}\times\Omega^d} + \frac{\mu}{2}\left\|l^{\mathrm{Tx}}\right\|^2_{\Omega^{\mathrm{Tx}}}\left\|l^{\mathrm{Rx}}\right\|^2_{\Omega^{\mathrm{Rx}}}\left\|f\right\|^2_{\Omega^{\mathrm{mid}}\times\Omega^d}. \quad (24)$$

In a second time, Algorithm 1 rescales the solutions of (24) to recover the solutions of the constrained problem (19). The unit constraints on the aberration vectors ensure that the amplitude of f remains consistent between different window positions. To the best of our knowledge, there exists no proof of convergence for ALS in the present case of weighted CP decomposition. Convergence guarantees exist however for the unweighted regularized case [39]. Even if we are not certain that ALS converges to a global minimum, we are guaranteed that it will converge to a local minimum that is at least as good—with respect to the loss—as the case where l^{Tx} and l^{Rx} are uniform.

In practice, we need to discretize l^{Tx}, l^{Rx}, and f. First of all, we can naturally express l^{Tx} as a vector $\boldsymbol{l}^{\mathrm{Tx}} \in \mathbb{C}^{N^{\mathrm{Tx}}}$. In addition, we can determine the discrete Rx angles $\boldsymbol{\theta}^{\mathrm{Rx}} \in \mathbb{R}^{N^{\mathrm{Rx}}}$ and mid angles $\boldsymbol{\theta}^{\mathrm{mid}} \in \mathbb{R}^{N^{\mathrm{mid}}}$ such that interpolation can be avoided in the implementation of Algorithm 1. To do so, the Tx and Rx angular spacings should be multiples of one another and the angular spacing of $\boldsymbol{\theta}^{\mathrm{mid}}$ should be half of the minimum of the Tx and Rx angular spacings. Consequently, we can infer that $\boldsymbol{\theta}^{\mathrm{Rx}} = [-35°, -32.5°, ..., 35°]$, since the angular spacing must be inferior to 3.82° in accordance with Section III-C, and that $\boldsymbol{\theta}^{\mathrm{mid}} = [-27.5°, -26.25°, ..., 27.5°]$, since the maximum mid angle is given by $(35°+20°)/2 = 27.5°$, namely the average between the maximum Tx and Rx

Algorithm 1: Alternating Least Squares

$l^{\mathrm{Tx}}(\theta^{\mathrm{Tx}}) \leftarrow 1$;
$l^{\mathrm{Rx}}(\theta^{\mathrm{Rx}}) \leftarrow 1$;
for $i := 1$ *to* N^{iter} **do**
  $f(\theta^{\mathrm{mid}}, d) \leftarrow \frac{2\int_{\theta^{\mathrm{Tx}}} \bar{l}^{\mathrm{Tx}}(\theta^{\mathrm{Tx}}) \bar{l}^{\mathrm{Rx}}(2\theta^{\mathrm{mid}}-\theta^{\mathrm{Tx}}) s(\theta^{\mathrm{Tx}}, 2\theta^{\mathrm{mid}}-\theta^{\mathrm{Tx}}, d)\,\mathrm{d}\theta^{\mathrm{Tx}}}{2\int_{\theta^{\mathrm{Tx}}} \left|l^{\mathrm{Tx}}(\theta^{\mathrm{Tx}}) l^{\mathrm{Rx}}(2\theta^{\mathrm{mid}}-\theta^{\mathrm{Tx}})\right|^2 \mathrm{d}\theta^{\mathrm{Tx}} + \mu \left\|l^{\mathrm{Tx}}\right\|^2_{\Omega^{\mathrm{Tx}}} \left\|l^{\mathrm{Rx}}\right\|^2_{\Omega^{\mathrm{Rx}}}}$;
  $l^{\mathrm{Tx}}(\theta^{\mathrm{Tx}}) \leftarrow \frac{\iint_{\theta^{\mathrm{Rx}},d} \bar{f}\left(\frac{\theta^{\mathrm{Tx}}+\theta^{\mathrm{Rx}}}{2}, d\right) \bar{l}^{\mathrm{Rx}}(\theta^{\mathrm{Rx}}) s(\theta^{\mathrm{Tx}}, \theta^{\mathrm{Rx}}, d)\,\mathrm{d}\theta^{\mathrm{Rx}}\,\mathrm{d}d}{\iint_{\theta^{\mathrm{Rx}},d} \left|f\left(\frac{\theta^{\mathrm{Tx}}+\theta^{\mathrm{Rx}}}{2}, d\right) l^{\mathrm{Rx}}(\theta^{\mathrm{Rx}})\right|^2 \mathrm{d}\theta^{\mathrm{Rx}}\,\mathrm{d}d + \mu \left\|l^{\mathrm{Rx}}\right\|^2_{\Omega^{\mathrm{Rx}}} \left\|f\right\|^2_{\Omega^{\mathrm{mid}}\times\Omega^d}}$;
  $l^{\mathrm{Rx}}(\theta^{\mathrm{Rx}}) \leftarrow \frac{\iint_{\theta^{\mathrm{Tx}},d} \bar{f}\left(\frac{\theta^{\mathrm{Tx}}+\theta^{\mathrm{Rx}}}{2}, d\right) \bar{l}^{\mathrm{Tx}}(\theta^{\mathrm{Tx}}) s(\theta^{\mathrm{Tx}}, \theta^{\mathrm{Rx}}, d)\,\mathrm{d}\theta^{\mathrm{Tx}}\,\mathrm{d}d}{\iint_{\theta^{\mathrm{Tx}},d} \left|f\left(\frac{\theta^{\mathrm{Tx}}+\theta^{\mathrm{Rx}}}{2}, d\right) l^{\mathrm{Tx}}(\theta^{\mathrm{Tx}})\right|^2 \mathrm{d}\theta^{\mathrm{Tx}}\,\mathrm{d}d + \mu \left\|l^{\mathrm{Tx}}\right\|^2_{\Omega^{\mathrm{Tx}}} \left\|f\right\|^2_{\Omega^{\mathrm{mid}}\times\Omega^d}}$;
end
$n^{\mathrm{Tx}} = \left\|l^{\mathrm{Tx}}\right\|_{\Omega^{\mathrm{Tx}}}$;
$n^{\mathrm{Rx}} = \left\|l^{\mathrm{Rx}}\right\|_{\Omega^{\mathrm{Rx}}}$;
$l^{\mathrm{Tx}}(\theta^{\mathrm{Tx}}) \leftarrow \frac{l^{\mathrm{Tx}}(\theta^{\mathrm{Tx}})}{n^{\mathrm{Tx}}}$;
$l^{\mathrm{Rx}}(\theta^{\mathrm{Rx}}) \leftarrow \frac{l^{\mathrm{Rx}}(\theta^{\mathrm{Rx}})}{n^{\mathrm{Rx}}}$;
$f(\theta^{\mathrm{mid}}, d) \leftarrow n^{\mathrm{Tx}} n^{\mathrm{Rx}} f(\theta^{\mathrm{mid}}, d)$;
Return: f, l^{Tx}, l^{Rx}

angles. Practically, only a few iterations are necessary in order for ALS to converge, in particular we set N^{iter}=20. Moreover, ALS is computationally light and easily parallelizable, as long as interpolation can be avoided in its implementation. Its computational complexity follows $O\left(N^{\mathrm{iter}} N^d N^{\mathrm{mid}}\right)$ and the time complexity of its GPU implementation can be reduced to $O\left(N^{\mathrm{iter}} \log\left(N^d N^{\mathrm{mid}}\right)\right)$. Ultimately, Algorithm 1 is run for each window position $\boldsymbol{r}^{\mathrm{w}}_{p,q}$.

E. Image Reconstruction

Once a single sinogram f per window position is obtained using Algorithm 1, we recover an estimation of a local patch by applying the backprojection operator $\mathcal{R}^*$ to f, namely

$$y^{\mathrm{f,\,P}}(\boldsymbol{r}', \boldsymbol{r}^{\mathrm{w}}) = \mathcal{R}^*_{(\theta^{\mathrm{mid}}, d)} \left\{f(\theta^{\mathrm{mid}}, d, \boldsymbol{r}^{\mathrm{w}})\right\}(\boldsymbol{r}' - \boldsymbol{r}^{\mathrm{w}}), \quad (25)$$

in the continuous domain. Backprojection is then repeated for each window position $\boldsymbol{r}^{\mathrm{w}}_{p,q}$.

As a final step, the patches obtained with (25) need to be assembled into a single CRF image y^{f}. Unfortunately, the value of f for each window position $\boldsymbol{r}^{\mathrm{w}}$ is recovered up to an arbitrary phase. We must therefore make sure that the patches are added up in phase, otherwise detrimental artifacts are likely to appear. We thus perform the image reconstruction using Algorithm 2, where patches are added to the image y^{f} after a phase correction v that is updated $N^{\mathrm{iter,\,out}}$ times. $N^{\mathrm{iter,\,out}}$ is set to 10 in practice. Moreover, we compute a normalization factor n to correct magnitude variations induced by windowing. The corrected image y^{f} is discretized as a vector $\boldsymbol{y}^{\mathrm{f}} \in \mathbb{C}^{N^x N^z}$, using

Algorithm 2: Image Reconstruction

$y^{\mathrm{f}}(\boldsymbol{r}') \leftarrow 0$;
$n(\boldsymbol{r}') \leftarrow 0$;
for $p := 1$ *to* $N^{w,x}$ *and* $q := 1$ *to* $N^{w,z}$ **do**
  $y^{\mathrm{f,\,w}}(\boldsymbol{r}', \boldsymbol{r}^{\mathrm{w}}_{p,q}) \leftarrow w(\boldsymbol{r}' - \boldsymbol{r}^{\mathrm{w}}_{p,q}) y^{\mathrm{f,\,P}}(\boldsymbol{r}', \boldsymbol{r}^{\mathrm{w}}_{p,q})$;
  $n(\boldsymbol{r}') \leftarrow n(\boldsymbol{r}') + w^2(\boldsymbol{r}' - \boldsymbol{r}^{\mathrm{w}}_{p,q})$;
  $y^{\mathrm{f}}(\boldsymbol{r}') \leftarrow y^{\mathrm{f}}(\boldsymbol{r}') + y^{\mathrm{f,\,w}}(\boldsymbol{r}', \boldsymbol{r}^{\mathrm{w}}_{p,q})$;
end
for $i := 1$ *to* $N^{iter,\,out}$ **do**
  for $p := 1$ *to* $N^{w,x}$ *and* $q := 1$ *to* $N^{w,z}$ **do**
    $y^{\mathrm{f},0}(\boldsymbol{r}') \leftarrow y^{\mathrm{f}}(\boldsymbol{r}') - y^{\mathrm{f,\,w}}(\boldsymbol{r}', \boldsymbol{r}^{\mathrm{w}}_{p,q})$;
    $v \leftarrow \int_{\boldsymbol{r}'} y^{\mathrm{f},0}(\boldsymbol{r}') \bar{y}^{\mathrm{f,\,w}}(\boldsymbol{r}', \boldsymbol{r}^{\mathrm{w}}_{p,q})\,\mathrm{d}\boldsymbol{r}'$;
    $y^{\mathrm{f,\,w}}(\boldsymbol{r}') \leftarrow \frac{v}{|v|} y^{\mathrm{f,\,w}}(\boldsymbol{r}')$;
  end
  $y^{\mathrm{f}}(\boldsymbol{r}') \leftarrow 0$;
  for $p := 1$ *to* $N^{w,x}$ *and* $q := 1$ *to* $N^{w,z}$ **do**
    $y^{\mathrm{f}}(\boldsymbol{r}') \leftarrow y^{\mathrm{f}}(\boldsymbol{r}') + y^{\mathrm{f,\,w}}(\boldsymbol{r}', \boldsymbol{r}^{\mathrm{w}}_{p,q})$;
  end
end
$y^{\mathrm{f}}(\boldsymbol{r}') = \frac{y^{\mathrm{f}}(\boldsymbol{r}')}{n(\boldsymbol{r}')}$;
Return: y^{f}

the same grid than the initial images $\boldsymbol{y}^{\mathrm{DAS}}$. The brightness (B)-mode image is ultimately computed as

$$y^{\mathrm{f,\,B}}(\boldsymbol{r}') = 20 \log_{10} \left|y^{\mathrm{f}}(\boldsymbol{r}')\right|. \quad (26)$$

A visual summary of the proposed method is depicted in Figure 1.

F. SVD Beamforming

To compare the performance of our approach to a state-of-the art method, the SVD beamformer proposed in [20] is implemented. The choice of the SVD beamformer is motivated by its compatibility with the proposed PW sequence and its conceptual similarities with our method. However, we must highlight that the Tx-only correction performed by SVD beamforming allows for a computationally lighter method.

The implementation is performed as follows. First, we define w^{SVD} as a square window, such that the multiplication of an image with w^{SVD} shifted by $\boldsymbol{r}^w$ corresponds to a patch extraction. Consequently, we can solve the following inverse problem

$$\underset{y^{\mathrm{f,\,P}}, \|l^{\mathrm{Tx}}\|=1}{\arg\min} \int_{\boldsymbol{r}'} \int_{\theta^{\mathrm{Tx}}} \left|y^{\mathrm{f,\,P}}(\boldsymbol{r}') l^{\mathrm{Tx}}(\theta^{\mathrm{Tx}}) - y^{\mathrm{DAS}}(\theta^{\mathrm{Tx}}, \boldsymbol{r}') w^{\mathrm{SVD}}(\boldsymbol{r}' - \boldsymbol{r}^w)\right|^2 \mathrm{d}\theta^{\mathrm{Tx}}\,\mathrm{d}\boldsymbol{r}', \quad (27)$$

for all the patch positions $\boldsymbol{r}^{\mathrm{w}}$. The solution of (27) is a function $y^{\mathrm{f,\,P}}(\boldsymbol{r}', \boldsymbol{r}^w)$ that can be directly used by Algorithm 2 with $w = w^{\mathrm{SVD}}$ to reconstruct the corrected image y^{f}. Similarly to the proposed method, y^{DAS}, $y^{\mathrm{f,\,P}}$ and l^{Tx} can be represented by discrete complex vectors. The solution of (27) is thus given

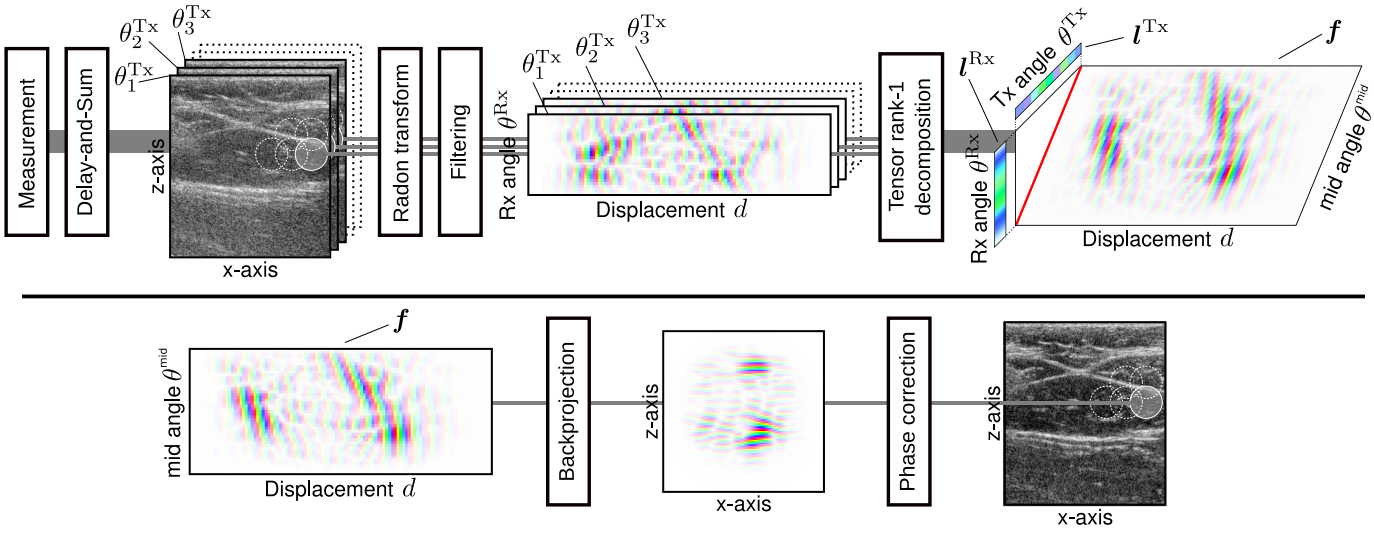

Fig. 1. Summary of the proposed method. Top row: beamforming of a single complex radio-frequency image per insonification, followed by windowed Radon transform and filtering. Tensor rank-1 decomposition is then performed patch-wise according to (19) and Algorithm 1. The phase and magnitude of complex numbers are encoded by the hue and darkness of the depicted colors, respectively. Bottom row: reconstruction of a patch from the result of tensor decomposition, followed by the reconstruction of the output image from the whole set of patches according to Algorithm 2.

by the two leading singular vectors of the windowed series of images expressed as a matrix.

We set the parameters of the SVD beamformer to be as close as possible to the ones of the proposed method to ensure a meaningful comparison. In particular the half-side of a square patch is identical to the window radius R^{w} (2 mm) and the same distance between patch centers is kept.

IV. Experiments

In this section, we detail the experiments we perform to check the validity of the proposed method and present their results. We also compare our method to standard coherent compounding and SVD beamforming. We first assess quantitatively the proposed method using simulated data, followed by tests of the method with in-vitro and in-vivo data.

A. Simulation

We depict in Figure 2a, the numerical phantom designed to quantitatively assess the performance of our method. A SoS of $1540\,\mathrm{m\,s^{-1}}$ is set in the phantom background. Two inclusions—one anechoic and one hypoechoic 6dB below the background echogeneicity—and six scatterers are embedded within the medium. Moreover, we add an irregular aberrating layer with a SoS of $1500\,\mathrm{m\,s^{-1}}$ and an echogeneicity 6dB above the background on top of the phantom. In particular, the lower boundary of the aberrating layer is defined as

$$z^{\max}(x)\ [\mathrm{mm}] = 9 + 1.5\cos(2\pi x/16). \tag{28}$$

We choose such a layer—in opposition to a flat layer or a phase screen—for its capacity to generate complex phase aberrations with strong lateral variations. Complex laterally-varying aberrations can typically occur in the imaging of the abdominal wall due to the interweave of muscle and fat tissues. We simulated using k-Wave [40] the data corresponding to 10 different speckle realisations of the phantom.

In addition, figure 2a presents the zones considered to evaluate the performance of our method. As detailed below, four different features have been analyzed: contrast, scatterer resolution, speckle statistics, and the ability to accurately correct aberrations.

- To compare contrast, we compute the contrast ratio (CR) between the two inclusions and their adjacent backgrounds. The inclusions' interiors used to estimate the CRs are highlighted with purple and green lines and the backgrounds are bounded by lighter lines. To account for the apparent position displacement due to the aberrating layer, the centers of both inclusions are shifted by 200 µm along the z-axis in the coherent compounding, SVD beamforming and proposed method cases.
- To compare resolution, we compute the axial and lateral full width at half maximum (FWHM) of near and far field scatterers. They are displayed in red and orange in Figure 2a, respectively.
- To check if the first-order statistical properties of speckle pattern are maintained by the proposed method, we test how much the speckle patterns generated by the different methods fit a Rayleigh distribution [41]. We perform Kolmogorov-Smirnov (KS) tests between the measured distributions of pixel magnitudes within the blue rectangle in Figure 2a and Rayleigh distributions fitted with a maximum likelihood estimator.
- Lastly, we check whether the proposed method is able to correctly compensate for Tx and Rx aberrations and recover speckle patterns coherent with a theoretical unaberrated image. To do so, we generate a reference image with DAS and coherent compounding from a simulation without the top aberrating layer. We then compute the maximum of the normalized cross-correlation between a series of patches extracted from the target CRF image and the corresponding patches in the reference CRF

TABLE II
SIMULATION RESULTS

	Coherent compounding	SVD beamforming	Proposed method	Reference
Anechoic CR [dB]	-18.83 (0.33)	-22.08 (0.39)	-25.08 (0.36)	-22.95 (0.36)
Hypoechoic CR[a] [dB]	-5.86 (0.23)	-6.12 (0.33)	-6.29 (0.26)	-6.04 (0.27)
Near-field lateral FWHM [μm]	594 (29)	641 (28)	247 (4)	244 (2)
Near-field axial FWHM [μm]	199 (3)	200 (6)	211 (4)	210 (4)
Far-field lateral FWHM [μm]	333 (19)	333 (10)	260 (6)	280 (6)
Far-field axial FWHM [μm]	220 (3)	218 (3)	204 (3)	206 (4)
Normalized cross-correlation	0.768 (0.085)	0.796 (0.072)	0.951 (0.027)	×[b]
Speckle Rayleigh KS test [10^{-3}]	9.35 (4.17)	8.78 (4.02)	6.97 (2.31)	7.06 (2.15)

[a]Target value: -6dB
[b]The cross-correlation is computed with respect to the reference image

aberration-free image. The patches selected to perform this analysis present speckle patterns that are especially aberrated in the coherent compounding images. These patches are highlighted in blue in Figure 2a.

Figures 2b-2d depict the results of coherent compounding, SVD beamforming and the proposed method using data from a single speckle realisation of the phantom. Close-ups of a near-field and a far-field scatterers (in red and orange in figure 2a) are also presented in the bottom row. Figure 2e displays the reference aberration-free image. Furthermore, we summarize in Table II the different metrics, averaged over 10 speckle realisations of the phantom. The standard deviation is given between parentheses.

From the results presented in Table II, we can observe that the most noticeable benefit of the proposed method with respect to coherent compounding and SVD beamforming is its capacity to accurately reconstruct scatterers. As depicted in the close-ups of Figure 2, the SVD beamformer improves the quality of the far-field scatterer—even if it is not reflected on its lateral FWHM—but fails to correct the near-field scatterer. On the contrary, the proposed method recovers scatterers that are qualitatively and quantitatively comparable to the ones of the reference image. Nevertheless, we can notice that the axial displacement in the apparent positions of the scatterers compared to the reference image is not compensated by the SVD beamforming and the proposed method.

Regarding the anechoic inclusion, we can notice that both SVD beamforming and the proposed method provide contrast improvements compared to coherent compounding. The proposed method achieves however a better contrast ratio—even outperforming the contrast ratio of the reference image—and a better reconstruction of the inclusion's shape. With regard to the hypoehoic inclusion, all four methods achieve similar average contrast ratios with similar standard deviations.

Finally, from the normalized cross-correlation with the reference image, we observe that our method highly outperforms SVD beamforming and coherent compounding. The SVD beamformer allows only a limited improvement compared to coherent compounding. In contrast, the image reconstructed using the proposed method consistently correlates with the reference image to a high degree, thus accurately compensating for aberrations and maintaining speckle coherence. The proposed method also maintains the speckle statistics with respect to the reference image. A slight improvement compared to the reference methods can be observed, but the uncertainty of the results prevents any conclusion.

B. Regularization Parameter

One of the key enablers of our method is the regularization parameter. To quantify its impact on imaging quality, we reconstruct the images corresponding to the 10 speckle realizations of the phantom with different values of the regularization parameter μ. We present in Figure 3 the evolution of the metrics—at the exception of axial resolution of the scatterers which is only weakly affected by the aberrations, as seen in Table II—with respect to μ. We depict in the same figure the metrics associated with coherent compounding, SVD beamforming and the reference image, which are all independent from the regularization parameter. The plain lines and shaded areas represent the mean and standard deviation of the metrics over the 10 speckle realisations, respectively.

We can notice that the trade-off between resolution and robustness described in Section III-D is confirmed experimentally. Indeed, the lower the regularization parameter is, the smaller the lateral resolution becomes. The resolution of the reference image is even outperformed with both the near and far-field scatterers when $\mu < 1$. By contrast, the contrast ratios of the anechoic inclusion—and to a lesser degree the hypoechoic inclusion—worsen, a sign that the proposed method becomes more sensitive to diffraction and multiple scattering artifacts. This sensitivity to artifacts can also be observed on the normalized cross-correlation, since it also decreases when μ diminishes. The change in cross-correlation cannot however be solely explained by the presence of artifacts since the speckle is tightened when μ decreases. For illustration, we depict in Figure 4 a scatterer and the anechoic inclusion for three values of μ, along with the reference image. Finally, no significant variation can be observed regarding the fitting of the speckle pattern to a Rayleigh distribution.

To conclude, we determine the default regularization parameter $\mu = 1$ as the value at which the lateral resolution achieved by the proposed method is at least equal to the one of the reference image.

C. Number of Insonifications

We also test the influence of the number of insonifications on the quality of the images. To do so, we perform additional simulations, varying for each new sequence the number of PWs emitted N^{Tx} but keeping the same steering angle range, namely $-20°$ to $20°$. The number of PWs considered N^{Tx} ranges from 5 to 80, since the result of the proposed method are incoherent if $N^{\mathrm{Tx}} < 5$. We believe this limit arises when

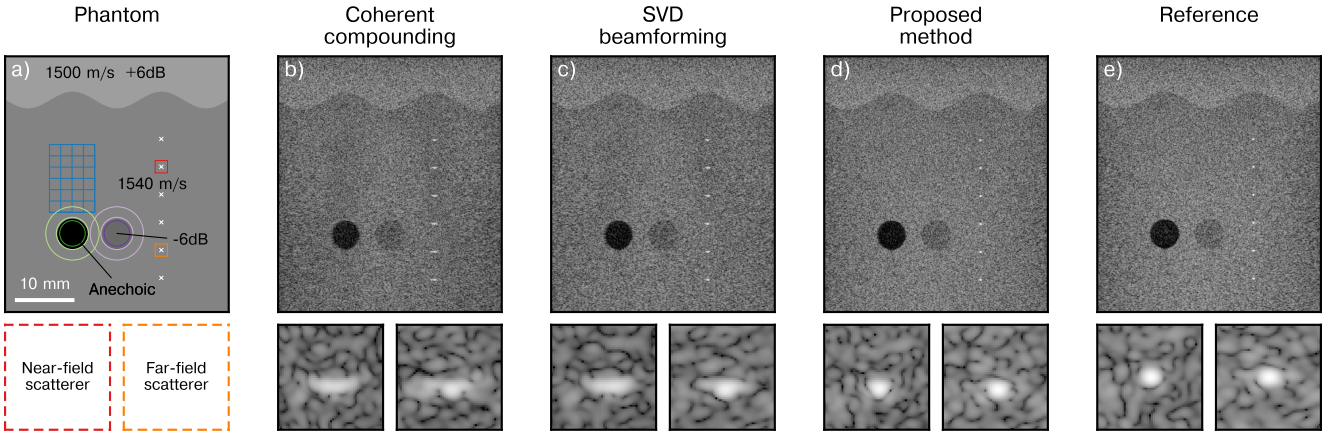

Fig. 2. Top row: B-mode images reconstructed from simulated data depicted with a 60 dB dynamic range, bottom row: examples of scatterers. a) Phantom geometry with the top aberrating layer and the zones considered for the computation of the metrics highlighted. b) Coherent compounding image reconstructed from a single speckle realisation of the phantom. c) Result of the SVD beamformer. d) Result of the proposed method. e) Reference coherent compounding image obtained from data simulated without the aberrating layer.

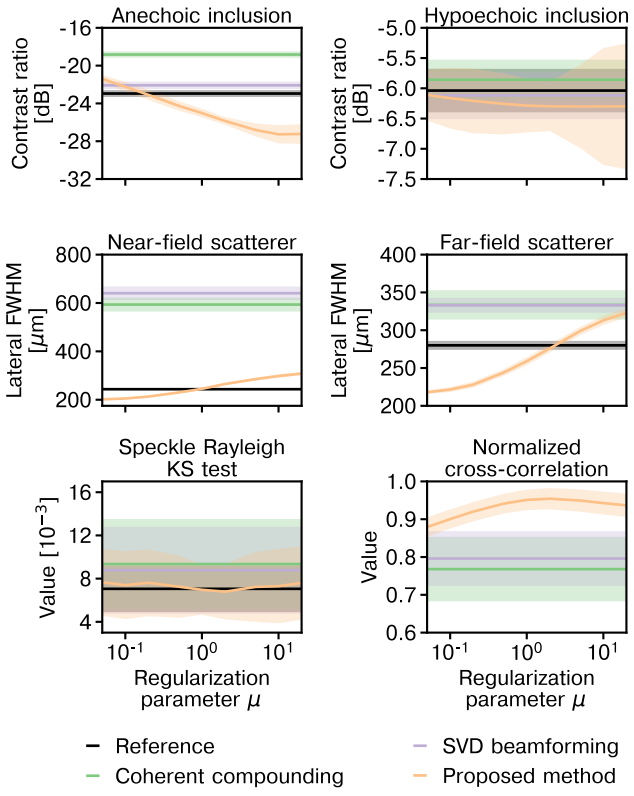

Fig. 3. Influence of the regularization parameter μ on the average image quality metrics. The metrics are computed over 10 speckle realizations of the phantom and depicted with their standard deviations.

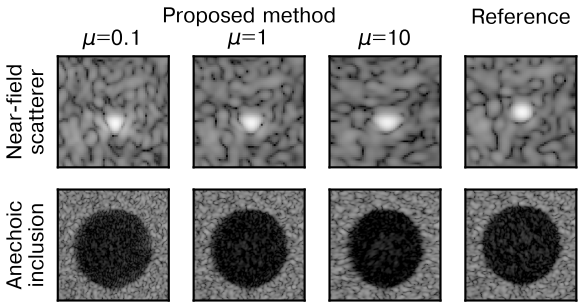

Fig. 4. B-mode examples of scatterer and anechoic inclusion reconstructed using different values of the regularization parameter μ. They are compared with a reference aberration-free image and displayed with a 60 dB dynamic range.

the number of unknowns in (19) is too large in comparison with the size of the available data.

Figure 5 represents the contrasts, speckle distribution, and speckle correlation with respect to the number of PWs considered N^{Tx}. The plain lines and shaded areas represent the mean and standard deviation of the metrics over the 10 speckle realisations, respectively. The scatterers' FWHMs are omitted due to the limited influence of the amount of PWs. With regard to the proposed method, both the Rx angles $\boldsymbol{\theta}^{\mathrm{Rx}}$ and mid angles $\boldsymbol{\theta}^{\mathrm{mid}}$ are updated for each new number of transmit angles N^{Tx} to comply with the criteria disclosed in Section III-D.

From Figure 5, we can observe an improvement of the anechoic CR with the number of PWs, regardless of the method applied. Notably, the relative difference between the four cases stays approximately constant. A noteworthy exception occurs when $N^{\mathrm{Tx}} > 40$, the results of the proposed method become worse than the reference image. As the number of insonifications N^{Tx} grows, the number of mid angles N^{mid}, and therefore the size of f, must be increased to avoid interpolation in Algorithm 1. We believe that the size increase of f beyond the minimum size necessary for patch reconstruction likely increases the variance of the patch reconstruction. Therefore, the sensitivity of the result to noise and imaging artifacts relatively to the other methods is negatively impacted.

The influence of the number of PWs on the hypoechoic CR, speckle distribution, and speckle correlation is more limited. Nonetheless, an improved stability of the correlation with respect to N_{Tx} can be observed with SVD beamforming and the proposed method, especially when $N_{\mathrm{Tx}} < 10$. Overall, we can conclude that the proposed method does not require a specific range of PWs to be effective.

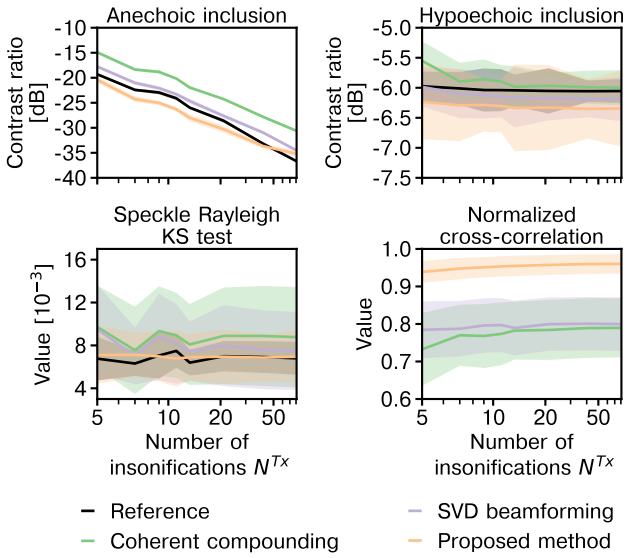

Fig. 5. Evolution of the average image quality metrics with respect to the number of insonifications. The metrics are computed over 10 speckle realizations of the phantom and depicted with their standard deviations.

D. In-vitro Phantom

In addition to simulated data, the proposed method is also assessed with data measured on an in-vitro phantom. We employ a CIRS model 054GS general-purpose ultrasound phantom (Sun Nuclear, Melbourne, FL, USA) figuring a series of scatterers embedded within uniform speckle. We perform 10 experiments, each consisting of $N^{\mathrm{Tx}} = 9$ PW insonifications. We move the transducer perpendicularly to the imaging plane between each experiment.

Since the previous experiments considered only a specific aberration severity, we propose to test the influence of the aberration delays on the performance of the proposed method. To do so, we simulate the presence of a thin uniform aberrating layer in front of the transducer by introducing Tx and Rx aberration delays during delay-and-sum. This approach was chosen, in opposition to a physical aberrator, to parameterize precisely the strength of the aberration. In fact, to investigate the behaviour of the proposed method to different aberration strength, we consider 21 aberration values—defined as the one-way aberration delay of an unsteered PW—ranging from $-1\,\mu$s to $1\,\mu$s. For each aberration value, we compare the results of coherent compounding with the proposed method using $\mu = 0.1$, $\mu = 1$, and $\mu = 10$ as regularization parameters. Unfortunately, we must disclose that the proposed aberrating layer does not capture the complex nature of in-vivo aberrations. A phantom study with physical aberrators can be performed in the future to further assess our method.

In line with Section IV-A, we compute the lateral FWHM of a mid-field scatterer—in orange in Figure 6a—and the maximum cross-correlation of a series of patches—in blue in Figure 6a—with respect to an unaberrated coherent compounding image. The results are depicted in Figure 6b and Figure 6e respectively, along with their standard deviation over the 10 experiments. In Figure 6f, we also depict the cross-correlation of the corrected image with the proposed

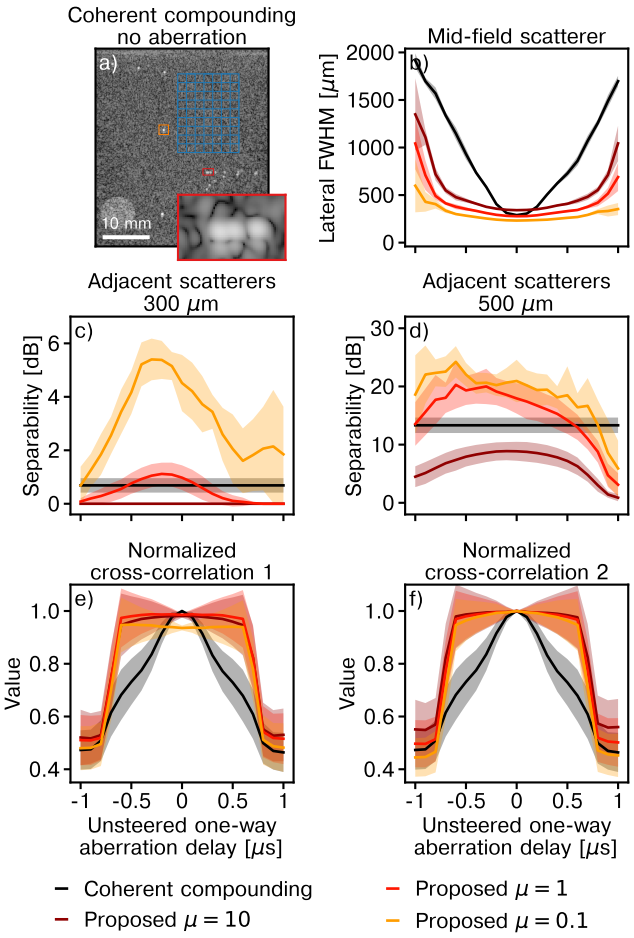

Fig. 6. In-vitro phantom results. a) Example of an unaberrated B-mode image with the zones considered for the metrics computation highlighted. b) Lateral FWHM of a mid-field scatterer with respect to the unsteered one-way aberration delay of the thin aberrating layer simulated during delay-and-sum. c) Separability of adjacent scatterers located at 300 μm from one another, for the unaberrated coherent compounding image and the images reconstructed with the proposed method. d) Separability of adjacent scatterers located at 500 μm from one another. e) Cross-correlation with unaberrated coherent-compounding images. f) Cross-correlation with the result of the proposed method applied to unaberrated data. The metrics are computed for 10 transducer positions and depicted along with their standard deviations.

method applied to unaberrated images. The resulting metric is therefore agnostic to the changes of speckle density induced by different regularizers μ. Furthermore, scatterer FWHM do not necessarily provide an accurate resolution metric in the case of non-linear beamformers [42]. To circumvent this issue, we compute the separability between three scatters—in red in Figure 6a—located at 300 µm and 500 µm from one another. The separability S between two scatterers located at positions $\boldsymbol{r}^1$ and $\boldsymbol{r}^2$ in a B-mode image y^{B} is defined as

$$S[dB] = \min\left\{y^{\mathrm{B}}(\boldsymbol{r}^1), y^{\mathrm{B}}(\boldsymbol{r}^2)\right\} - \min_{t\in[0,1]} y^{\mathrm{B}}\left(t\boldsymbol{r}^1 + (1-t)\boldsymbol{r}^2\right). \quad (29)$$

The influence of the aberration strength on the separability is depicted in Figure 6c and 6d, respectively, along with their standard deviation. Since separability is ill-defined for an aberrated image due to interferences between the aberrated

PSFs of the scatterers, we only depict the separability of the unaberrated coherent compounding image.

The main conclusion that can be drawn from Figure 6 is that the FWHM and cross-correlation concur to define a sharp boundary to the range of validity of the proposed method. This boundary occurs around an absolute aberration value of 0.6 µs to 0.7 µs. To put this value into perspective, it corresponds to the aberration delay generated by a 2 cm-thick layer of subcutaneous fat with SoS 1476 m s^{-1} [7]. The separability of the scatterers does not depict the same sharp transition but generally decreases with the aberration strength. We can notice that the separability values are coherent with the FWHM results and validate the resolution improvement allowed by the proposed method. Also, the resolution improvement with regard to coherent compounding, even without aberration, observed in Section IV-B for small values of the regularizer is confirmed by the scatterer separability. More generally, the conclusions obtained with simulated data are confirmed by the in-vitro phantom experiments.

E. In-vivo

To assess the in-vivo performance of the proposed method, we acquired two sets of data on the abdominal wall of a healthy volunteer (27 years old male), using 9 PW insonifications. The ultrasound sequence has been approved for research with human subjects by the Cantonal Ethics Committee of the Canton of Vaud, Switzerland. We reconstruct the images with coherent compounding, SVD beamforming and the proposed method, for both scanning positions. The resulting B-mode images are depicted in Figure 7, along with close-up of four areas of interest.

We can notice in each image the complex structure of the medium, with a series of non-parallel muscle and fat layers. Both types of layer typically possess distinct SoS, different from the expected c_0 =1540 m s^{-1} [7]. Therefore, the complex interweave of layers present in both scanning positions likely generates non-negligible aberrations.

We can first observe that the SVD beamformer and proposed method both improve contrast with respect to coherent compounding. The contrast improvement is especially visible in the median layer—between 2 and 3 cm—of both images and corroborates the results obtained with simulated data. However, the most noteworthy effect of the proposed method is its capacity to reconstruct scatterers. It can be observed in the top area of interest of the first image. An ovoidal scatterer is reconstructed, whereas it lacks definition with the two reference methods. It can also be seen in the bottom zone of interest of the second image. The proposed method reveals the presence of five scatterers whereas their presence can only be guessed from the two reference methods. Overall, our method permits a general qualitative improvement of the images. As an illustration, we can see in the top zone of interest of the second image the reconstruction of an interface, whereas it appears faint with coherent compounding or split in half with SVD beamforming.

V. Discussion

In this article, we introduce a novel adaptative beamforming method able to correct aberrations caused by SoS variations in the imaged medium. We show using simulated and in-vitro data that our method accurately corrects phase aberrations and recovers images that correlate to a high degree with ideal aberration-free images. In particular, the reduction in scatterer FWHM and the capacity to separate adjacent scatterers, confirm a large improvement in lateral resolution. We also establish that the proposed method allows a contrast improvement with respect to DAS even when aberration-free data are considered. Lastly, we present qualitative in-vivo results confirming, in particular, an improvement in scatterer resolution with regard to both coherent compounding and SVD beamforming.

A. Computation time and Generalizability

As desired, our method is highly parallelizable. Specifically, the bulk of the proposed technique can be performed simultaneously for each patch. The windowed Radon transform—the most computationally heavy operation of our method—can be parallelized further with respect to the Tx angles. The main temporal bottleneck is then given by the two iterative algorithms (Algorithms 1 and 2), but the numbers of iterations N^{iter} and $N^{\text{iter, out}}$ remain small in practice. Our prototype GPU implementation using 9PWs currently runs in 30 seconds on an Nvidia GeForce 2080 Ti GPU (Nvidia Corporation, Santa Clara, CA, USA). In particular, the computational time currently achieved by the proposed method do not compare with the one of the SVD beamformer, for which real-time computation has been reported [20]. The current implementation relies on Numba CUDA [43], a just-in-time GPU compiler of Python code. We consider that a *bona fide* CUDA implementation of the method can achieve a significant performance improvement with regard to the current implementation. In particular, the memory management can be greatly improved. The choice of the different parameters of the proposed method can also be optimized with computation time in mind. Overall, we believe that the computation time can be reduced to allow real-time image reconstruction.

More generally, we believe that the local PW basis proposed in this article is well-suited for limiting the computational complexity of local aberration correction. As discussed in Section III-C, restricting an image to a patch bounds the maximum angular resolution of its Radon transform. Selecting the Rx angles to approximate this bound leads to a reduction of data to process compared to an explicit spatial alignment of the measured signals [25]. Moreover, waves emitted using the transducer's full set of elements allow data acquisition with a high signal-to-noise ratio compared to a sequence of single-element insonifications. The number of insonifications, and thus the amount of data to process, can therefore be reduced compared to methods relying on the latter sequence.

We limit ourselves in this article to ultrafast PW imaging. However, both focused ultrasound imaging and ultrafast imaging using diverging waves suffer from the same SoS aberrations that the proposed method aims to correct. This

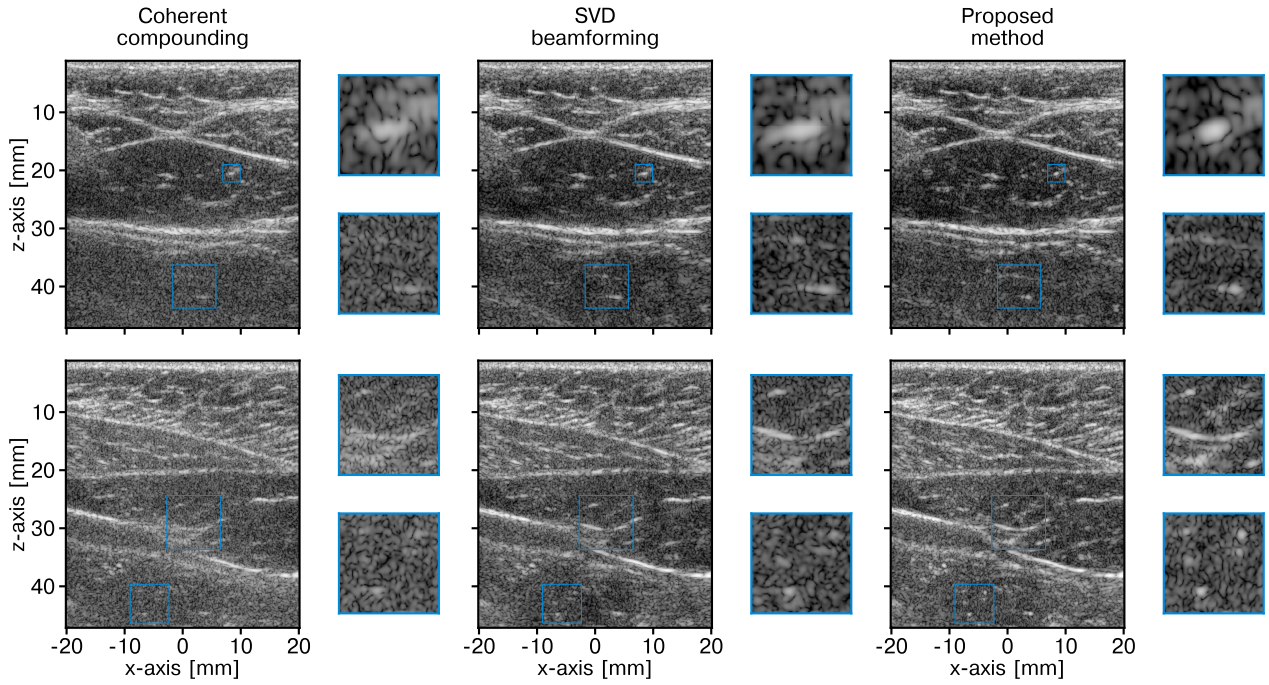

Fig. 7. Two in-vivo images of an abdominal wall (top and bottom row), using 9 plane wave insonifications and displayed with a 60 dB dynamic range. Results of coherent compounding, SVD beamforing and the proposed method are depicted. Areas of interest are highlighted in blue.

raises the question as to whether the proposed method can be used in these cases as well. The proposed theoretical framework can be easily adapted to other insonifications, with the caveat that the angles of the incident waves $\boldsymbol{\theta}^{\mathrm{Tx}}$ vary with the window position $\boldsymbol{r}^{\mathrm{w}}$. However, additional difficulties arise in the implementation of Algorithm 1. Since the Tx angles $\boldsymbol{\theta}^{\mathrm{Tx}}$ are not necessarily uniformly spaced anymore, the Rx angles $\boldsymbol{\theta}^{\mathrm{Rx}}$ and mid angles $\boldsymbol{\theta}^{\mathrm{mid}}$ cannot be selected to allow a direct discretization of Algorithm 1. Its performances are therefore expected to be ultimately impeded compared to PW imaging.

Nonetheless, the proposed method can be directly applied to data acquired with any linear transducer emitting a sequence of uniformly spaced PWs. The proposed image grid size $\Delta x = \Delta z$, distance between window centers $\Delta x^{\mathrm{w}} = \Delta z^{\mathrm{w}}$ and window Radius R^{w} are defined in function of the wavelength c_0/f_0. They must be therefore updated if the beamforming speed c_0 or the excitation frequency f_0 are changed. Moreover, the Rx apodization weights a^{Rx} and the maximum mid and Rx angles must also be updated according to the directivity of the transducer elements.

B. Limitations

According to the principle of acoustic reciprocity, the phases of the angular aberrations functions l^{Tx} and l^{Rx} are equal in theory (14). Moreover, their amplitude can also be assumed equal under mild hypotheses, provided matching Tx and Rx apodization functions. However, the proposed method fully disregards the principle of acoustic reciprocity and posits that the Tx and Rx aberrations are independent, in stark contrast with other recent Tx/Rx aberration correction methods [24], [25]. The rationale behind this choice is twofold:

1) Introducing a single aberration vector, or an equality constraint between the Tx and Rx aberration vectors, would complexify the minimization problem and prevent the use of ALS for its resolution.
2) Tissue movements may occur between insonifications and can be interpreted as Tx phase shifts. Considering distinct Tx and Rx aberrations likely provide additional robustness to in-vivo movement artifacts compared to methods positing identical Tx and Rx aberrations. This property can be especially relevant for applications where tissue displacements are expected, such as elastography, or when large numbers of insonifications are considered.

However, imposing the Tx and Rx aberrations to be equal—or penalizing their difference—can increase the robustness of the method if the tissue movements are negligible, especially when the number of PWs emitted is small. For example, considering a unique aberration vector could in theory extent the validity of the method to cases where $N^{\mathrm{Tx}} < 5$. Therefore, it would be of interest to seek an efficient way to integrate such a constraint into the proposed method. Comparisons could ultimately be performed to quantify the usefulness of the Tx-Rx splitting of aberrations, beyond the fact that it enables the use of ALS.

A fundamental limitation of the proposed method is its failure to retrieve the absolute position of reflective structures. This drawback arises from the estimation of time delays by phase shifts and from the inability of our method to recover the global phase of $\boldsymbol{l}^{\mathrm{Tx/Rx}}$. A reconstruction of the SoS map is therefore probably necessary to address this shortcoming. The parallelizability of such a method would however be impaired. The phase-shift hypothesis also limits the maximum aberration delay our method can correct, as seen in Section IV-D. The

applicability of our method to cases where strong aberrations are present is therefore hindered, including most probably transcranial imaging.

C. Applications

Since the proposed method is able to recover aberration vectors $\boldsymbol{l}^{\mathrm{Tx/Rx}}$ for a series of points in the medium, one can imagine using their magnitude and phase to recover the spatial distribution of attenuation and SoS, respecively. Unfortunately, we advise against the direct use of the proposed method to that end. First, it has been shown that the phase modulation neglected by the proposed method (8) is important for the accuracy of the measurement model in pulse-echo SoS imaging [13]. Second, the regularization term introduced in (19) tends to bias the magnitude of the aberration vectors $\boldsymbol{l}^{\mathrm{Tx/Rx}}$, therefore reducing their interest as a feature for attenuation imaging. Nonetheless, we believe that windowed Radon transform can act as a powerful framework for quantitative pulse-echo ultrasound imaging in the future, but that a different way to estimate local angular aberrations must be devised with this specific application in mind.

SoS aberrations affect the quality of displacement tracking between consecutive frames. The performances of methods such as shear-wave elastography are therefore diminished. A first possible application of the proposed method could be the improvement of displacement-tracking-based techniques as a consequence of our method's capacity to correct for Tx and Rx aberrations. Further reaserach is however necessary to quantify the impact of the proposed method in that case. Nonetheless, we can state that our method is useful to improve B-mode imaging, as indicated by both the controlled experiments and the in-vivo examples. Due to the low number of insonifications it requires, our method can be useful to improve the quality of ultrasound imaging with portable transducer since the amount of data they can acquire and transmit is likely to be limited. Finally, the proposed method can be especially relevant to the challenging case of overweight patients, since the presence of fat is likely to generate SoS aberrations and thus to impact negatively the diagnosis capability of ultrasound imaging [8], [9], [44].

Appendix I
Local Backprojection

Let us replace in (5) the measurements m and the expected transmisison times τ^{Tx}, τ^{Rx} by their definition according to (2), (3) and (7), respectively. The beamformed images can then be expressed locally as

$$y^{\mathrm{DAS}}\left(\theta^{\mathrm{Tx}}, \boldsymbol{r}'\right) \approx \int_{\theta^{\mathrm{Rx}}} l^{\mathrm{Tx}}\left(\theta^{\mathrm{Tx}}\right) l^{\mathrm{Rx}}\left(\theta^{\mathrm{Rx}}\right) \int_{\boldsymbol{r}} \gamma(\boldsymbol{r}) \\ v_{\mathrm{pe}}\left(\frac{2}{c_0}\cos\left(\frac{\theta^{\mathrm{Tx}}-\theta^{\mathrm{Rx}}}{2}\right)\left\langle \boldsymbol{u}\left(\frac{\theta^{\mathrm{Tx}}+\theta^{\mathrm{Rx}}}{2}\right), \boldsymbol{r}'-\boldsymbol{r}\right\rangle\right) \mathrm{d}\boldsymbol{r}\,\mathrm{d}\theta^{\mathrm{Rx}}, \quad (30)$$

where l^{Tx} and l^{Rx} are the aberration/apodization functions introduced in (14). We propose to perform the following change of variable

$$\boldsymbol{r} = \boldsymbol{r}^{\mathrm{w}} + \alpha^{\parallel}\boldsymbol{u}\left(\frac{\theta^{\mathrm{Tx}}+\theta^{\mathrm{Rx}}}{2}\right) + \alpha^{\perp}\boldsymbol{u}^{\perp}\left(\frac{\theta^{\mathrm{Tx}}+\theta^{\mathrm{Rx}}}{2}\right), \quad (31)$$

where $\boldsymbol{u}^{\perp}$ denotes a vector perpendicular to $\boldsymbol{u}$ and $\alpha^{\parallel}$ and $\alpha^{\perp}$ are integration variables along the directions given by $\boldsymbol{u}$ and $\boldsymbol{u}^{\perp}$, respectively. Taking (8) into account, (30) can therefore be rewritten as

$$y^{\mathrm{DAS}}\left(\theta^{\mathrm{Tx}}, \boldsymbol{r}'\right) \approx \int_{\theta^{\mathrm{Rx}}} l^{\mathrm{Tx}}\left(\theta^{\mathrm{Tx}}\right) l^{\mathrm{Rx}}\left(\theta^{\mathrm{Rx}}\right) \int_{\alpha^{\parallel}} \\ v_{\mathrm{pe}}\left(\frac{2}{c_0}\left[\left\langle \boldsymbol{u}\left(\frac{\theta^{\mathrm{Tx}}+\theta^{\mathrm{Rx}}}{2}\right), \boldsymbol{r}'-\boldsymbol{r}^{\mathrm{w}}\right\rangle - \alpha^{\parallel}\right]\right) \\ \int_{\alpha^{\perp}} \gamma\left(\alpha^{\parallel}\boldsymbol{u}\left(\theta^{\mathrm{mid}}\right) + \alpha^{\perp}\boldsymbol{u}^{\perp}\left(\theta^{\mathrm{mid}}\right) + \boldsymbol{r}^{\mathrm{w}}\right) \mathrm{d}\alpha^{\perp}\,\mathrm{d}\alpha^{\parallel}. \quad (32)$$

We introduce the intermediary variable

$$d = \left\langle \boldsymbol{u}\left(\frac{\theta^{\mathrm{Tx}}+\theta^{\mathrm{Rx}}}{2}\right), \boldsymbol{r}'-\boldsymbol{r}^{\mathrm{w}}\right\rangle \quad (33)$$

as the distance between the image position $\boldsymbol{r}'$ and $\boldsymbol{r}^{\mathrm{w}}$ along the direction given by $\boldsymbol{u}$. Equation (32) is then equivalent to

$$y^{\mathrm{DAS}}\left(\theta^{\mathrm{Tx}}, \boldsymbol{r}'\right) \approx \int_{\theta^{\mathrm{Rx}}} \\ s\left(\theta^{\mathrm{Tx}}, \theta^{\mathrm{Rx}}, \left\langle \boldsymbol{u}\left(\frac{\theta^{\mathrm{Tx}}+\theta^{\mathrm{Rx}}}{2}\right), \boldsymbol{r}'-\boldsymbol{r}^{\mathrm{w}}\right\rangle\right) \mathrm{d}\theta^{\mathrm{Rx}} \quad (34)$$

with

$$s\left(\theta^{\mathrm{Tx}}, \theta^{\mathrm{Rx}}, d\right) = l^{\mathrm{Tx}}\left(\theta^{\mathrm{Tx}}\right) l^{\mathrm{Rx}}\left(\theta^{\mathrm{Rx}}\right) f\left(\frac{\theta^{\mathrm{Tx}}+\theta^{\mathrm{Rx}}}{2}, d\right), \quad (35)$$

and

$$f\left(\theta^{\mathrm{mid}}, d\right) = \int_{\alpha^{\parallel}} v_{\mathrm{pe}}\left(\frac{2}{c_0}\left(d-\alpha^{\parallel}\right)\right) \\ \int_{\alpha^{\perp}} \gamma\left(\alpha^{\parallel}\boldsymbol{u}\left(\theta^{\mathrm{mid}}\right) + \alpha^{\perp}\boldsymbol{u}^{\perp}\left(\theta^{\mathrm{mid}}\right) + \boldsymbol{r}^{\mathrm{w}}\right) \mathrm{d}\alpha^{\perp}\,\mathrm{d}\alpha^{\parallel}. \quad (36)$$

Finally, (34) can be rewritten as (11) factoring in the definition of the backprojection operator (10).

Acknowledgment

The authors would like to thank Roser Vinals Terres for her re-reading, Baptiste Hériard-Dubreuil for his regular feedback, Thomas Deffieux for the helpful discussion, and Valentin Vuillon for his preliminary work on the method.

References

[1] M. Tanter and M. Fink, "Ultrafast imaging in biomedical ultrasound," *IEEE Transactions on Ultrasonics, Ferroelectrics, and Frequency Control*, vol. 61, no. 1, pp. 102–119, Jan. 2014.

[2] G. Montaldo, M. Tanter, J. Bercoff, N. Benech, and M. Fink, "Coherent plane-wave compounding for very high frame rate ultrasonography and transient elastography," *IEEE transactions on ultrasonics, ferroelectrics, and frequency control*, vol. 56, no. 3, pp. 489–506, 2009.

[3] L. Sandrin, M. Tanter, S. Catheline, and M. Fink, "Shear modulus imaging with 2-d transient elastography," *IEEE transactions on ultrasonics, ferroelectrics, and frequency control*, vol. 49, no. 4, pp. 426–435, 2002.

[4] M. Tanter, J. Bercoff, L. Sandrin, and M. Fink, "Ultrafast compound imaging for 2-d motion vector estimation: Application to transient elastography," *IEEE transactions on ultrasonics, ferroelectrics, and frequency control*, vol. 49, no. 10, pp. 1363–1374, 2002.

[5] J.-L. Gennisson, T. Deffieux, M. Fink, and M. Tanter, "Ultrasound elastography: Principles and techniques," *Diagnostic and Interventional Imaging*, vol. 94, no. 5, pp. 487–495, May 2013.

[6] C. Demené, J. Robin, A. Dizeux, B. Heiles, M. Pernot, M. Tanter, and F. Perren, "Transcranial ultrafast ultrasound localization microscopy of brain vasculature in patients," *Nature biomedical engineering*, vol. 5, no. 3, pp. 219–228, 2021.

[7] S. A. Goss, R. L. Johnston, and F. Dunn, "Comprehensive compilation of empirical ultrasonic properties of mammalian tissues," *The Journal of the Acoustical Society of America*, vol. 64, no. 2, pp. 423–457, Aug. 1978.

[8] J. J. Dahl, M. S. Soo, and G. E. Trahey, "Spatial and temporal aberrator stability for real-time adaptive imaging," *IEEE transactions on ultrasonics, ferroelectrics, and frequency control*, vol. 52, no. 9, pp. 1504–1517, 2005.

[9] G. E. Trahey and S. W. Smith, "Properties of acoustical speckle in the presence of phase aberration part I: first order statistics," *Ultrasonic Imaging*, vol. 10, no. 1, pp. 12–28, 1988.

[10] G. C. Ng, S. S. Worrell, P. D. Freiburger, and G. E. Trahey, "A comparative evaluation of several algorithms for phase aberration correction," *IEEE transactions on ultrasonics, ferroelectrics, and frequency control*, vol. 41, no. 5, pp. 631–643, 1994.

[11] S. Flax and M. O'Donnell, "Phase-aberration correction using signals from point reflectors and diffuse scatterers: Basic principles," *IEEE transactions on ultrasonics, ferroelectrics, and frequency control*, vol. 35, no. 6, pp. 758–767, 1988.

[12] M. O'donnell and S. Flax, "Phase-aberration correction using signals from point reflectors and diffuse scatterers: Measurements," *IEEE transactions on ultrasonics, ferroelectrics, and frequency control*, vol. 35, no. 6, pp. 768–774, 1988.

[13] P. Stähli, M. Kuriakose, M. Frenz, and M. Jaeger, "Improved forward model for quantitative pulse-echo speed-of-sound imaging," *Ultrasonics*, vol. 108, p. 106168, Dec. 2020.

[14] P. Stahli, M. Frenz, and M. Jaeger, "Bayesian approach for a robust speed-of-sound reconstruction using pulse-echo ultrasound," *IEEE Transactions on Medical Imaging*, vol. 40, no. 2, pp. 457–467, Feb. 2021.

[15] M. Jaeger, G. Held, S. Peeters, S. Preisser, M. Grünig, and M. Frenz, "Computed Ultrasound Tomography in Echo Mode for Imaging Speed of Sound Using Pulse-Echo Sonography: Proof of Principle," *Ultrasound in Medicine & Biology*, vol. 41, no. 1, pp. 235–250, Jan. 2015.

[16] S. J. Sanabria, E. Ozkan, M. Rominger, and O. Goksel, "Spatial domain reconstruction for imaging speed-of-sound with pulse-echo ultrasound: simulation and *in vivo* study," *Physics in Medicine & Biology*, vol. 63, no. 21, p. 215015, Oct. 2018.

[17] R. Ali and J. J. Dahl, "Distributed phase aberration correction techniques based on local sound speed estimates," in *2018 IEEE International Ultrasonics Symposium (IUS)*. IEEE, 2018, pp. 1–4.

[18] R. Rau, D. Schweizer, V. Vishnevskiy, and O. Goksel, "Ultrasound aberration correction based on local speed-of-sound map estimation," in *2019 IEEE International Ultrasonics Symposium (IUS)*. IEEE, 2019, pp. 2003–2006.

[19] M. Jaeger, E. Robinson, H. G. Akarçay, and M. Frenz, "Full correction for spatially distributed speed-of-sound in echo ultrasound based on measuring aberration delays via transmit beam steering," *Physics in Medicine and Biology*, vol. 60, no. 11, pp. 4497–4515, Jun. 2015.

[20] H. Bendjador, T. Deffieux, and M. Tanter, "The SVD beamformer: Physical principles and application to ultrafast adaptive ultrasound," *IEEE Transactions on Medical Imaging*, vol. 39, no. 10, pp. 3100–3112, Oct. 2020.

[21] H. Bendjador, S. Décombas-Deschamps, M. D. Burgio, R. Sartoris, B. Van Beers, V. Vilgrain, T. Deffieux, and M. Tanter, "The SVD beamformer with diverging waves: a proof-of-concept for fast aberration correction," *Physics in Medicine & Biology*, vol. 66, no. 18, p. 18LT01, 2021.

[22] H. Bendjador, T. Deffieux, and M. Tanter, "SVD beamforming for ultrafast aberration correction and real-time speed-of-sound quantification," in *2020 IEEE International Ultrasonics Symposium (IUS)*. Las Vegas, NV, USA: IEEE, Sep. 2020, pp. 1–4.

[23] W. Lambert, J. Robin, L. A. Cobus, M. Fink, and A. Aubry, "Ultrasound Matrix Imaging I. the focused reflection matrix, the f-factor and the role of multiple scattering." *IEEE Transactions on Medical Imaging*, 2022.

[24] W. Lambert, L. A. Cobus, J. Robin, M. Fink, and A. Aubry, "Ultrasound Matrix Imaging II. the distortion matrix for aberration correction over multiple isoplanatic patches." *IEEE Transactions on Medical Imaging*, 2022.

[25] G. Chau, M. Jakovljevic, R. Lavarello, and J. Dahl, "A locally adaptive phase aberration correction (LAPAC) method for synthetic aperture sequences," *Ultrasonic imaging*, vol. 41, no. 1, pp. 3–16, 2019, publisher: Sage Publications Sage CA: Los Angeles, CA.

[26] H.-M. Schwab and R. Lopata, "A Radon diffraction theorem for plane wave ultrasound imaging," *The Journal of the Acoustical Society of America*, vol. 153, no. 2, pp. 1015–1026, Feb. 2023.

[27] G. Jansen, N. Awasthi, H.-M. Schwab, and R. Lopata, "Enhanced radon domain beamforming using deep-learning-based plane wave compounding," in *2021 IEEE International Ultrasonics Symposium (IUS)*, 2021, pp. 1–4.

[28] H.-M. Schwab, F. Van De Vosse, and R. Lopata, "An r-space theorem for plane wave ultrasound reconstruction," in *2020 IEEE International Ultrasonics Symposium (IUS)*. IEEE, 2020, pp. 1–4.

[29] J. A. Jensen, "A model for the propagation and scattering of ultrasound in tissue," *The Journal of the Acoustical Society of America*, vol. 89, no. 1, pp. 182–190, 1991.

[30] A. Besson, D. Perdios, F. Martinez, Z. Chen, R. E. Carrillo, M. Arditi, Y. Wiaux, and J.-P. Thiran, "Ultrafast Ultrasound Imaging as an Inverse Problem: Matrix-Free Sparse Image Reconstruction," *IEEE Transactions on Ultrasonics, Ferroelectrics, and Frequency Control*, vol. 65, no. 3, pp. 339–355, Mar. 2018.

[31] A. Besson, L. Roquette, D. Perdios, M. Simeoni, M. Arditi, P. Hurley, Y. Wiaux, and J.-P. Thiran, "A physical model of nonstationary blur in ultrasound imaging," *IEEE Transactions on Computational Imaging*, vol. 5, no. 3, pp. 381–394, 2019.

[32] D. Perdios, M. Vonlanthen, F. Martinez, M. Arditi, and J.-P. Thiran, "CNN-based image reconstruction method for ultrafast ultrasound imaging," *IEEE Transactions on Ultrasonics, Ferroelectrics, and Frequency Control*, vol. 69, no. 4, pp. 1154–1168, 2021.

[33] T. L. Szabo, *Diagnostic ultrasound imaging: inside out*. Academic press, 2004.

[34] A. Selfridge, G. Kino, and B. Khuri-Yakub, "A theory for the radiation pattern of a narrow-strip acoustic transducer," *Applied Physics Letters*, vol. 37, no. 1, pp. 35–36, 1980.

[35] S. Helgason, *The radon transform*. Springer, 1980, vol. 2.

[36] G. Kaiser and R. F. Streater, "Windowed radon transforms, analytic signals, and the wave equation," *Wavelets: A tutorial in theory and applications*, pp. 399–441, 1992.

[37] N. Q. Nguyen and R. W. Prager, "A spatial coherence approach to minimum variance beamforming for plane-wave compounding," *IEEE Transactions on Ultrasonics, Ferroelectrics, and Frequency Control*, vol. 65, no. 4, pp. 522–534, Apr. 2018.

[38] J.-F. Synnevag, A. Austeng, and S. Holm, "Benefits of minimum-variance beamforming in medical ultrasound imaging," *IEEE Transactions on Ultrasonics, Ferroelectrics and Frequency Control*, vol. 56, no. 9, pp. 1868–1879, Sep. 2009.

[39] P. Comon, X. Luciani, and A. L. De Almeida, "Tensor decompositions, alternating least squares and other tales," *Journal of Chemometrics: A Journal of the Chemometrics Society*, vol. 23, no. 7-8, pp. 393–405, 2009.

[40] B. E. Treeby and B. T. Cox, "k-wave: Matlab toolbox for the simulation and reconstruction of photoacoustic wave fields," *Journal of biomedical optics*, vol. 15, no. 2, p. 021314, 2010.

[41] C. B. Burckhardt, "Speckle in ultrasound B-mode scans," *IEEE Transactions on Sonics and Ultrasonics*, vol. 25, no. 1, pp. 1–6, Jan. 1978.

[42] O. M. Hoel Rindal, A. Austeng, and A. Rodriguez-Molares, "Resolution measured as separability compared to full width half maximum for adaptive beamformers," in *2020 IEEE International Ultrasonics Symposium (IUS)*. Las Vegas, NV, USA: IEEE, Sep. 2020, pp. 1–4.

[43] S. K. Lam, A. Pitrou, and S. Seibert, "Numba: a LLVM-based Python JIT compiler," in *Proceedings of the Second Workshop on the LLVM Compiler Infrastructure in HPC*. Austin Texas: ACM, Nov. 2015, pp. 1–6.

[44] M. Maar, J. Lee, A. Tardi, Y.-Y. Zheng, C. Wong, and J. Gao, "Inter-transducer variability of ultrasound image quality in obese adults: Qualitative and quantitative comparisons," *Clinical Imaging*, vol. 92, pp. 63–71, 2022.